Article

Immunity

Resident macrophage-dependent immune cell scaffolds drive anti-bacterial defense in the peritoneal cavity

Graphical abstract

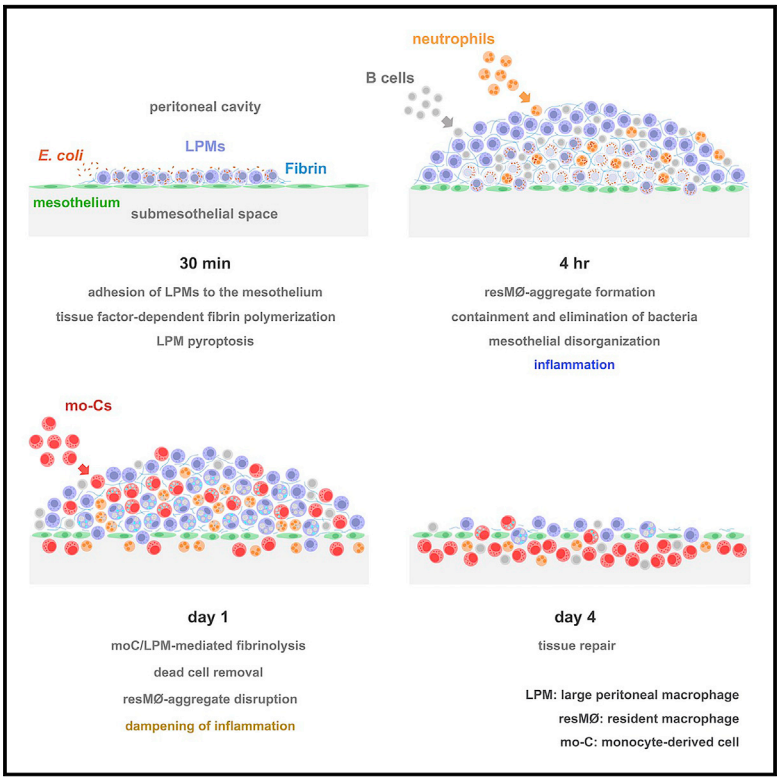

Highlights

- LPMs drive the defense against E. coli through the formation of resident macrophage aggregates
- Resident macrophage aggregates are mesothelium-bound, fibrin-dependent immune cell scaffolds
- During the resolution of infection, LPMs promote moC recruitment to resident macrophage aggregates
- moCs control inflammation through fibrinolysis-driven resident macrophage aggregate disaggregation

Authors

Adrián Vega-Pérez, Laura H. Villarrubia, Cristina Godio, ..., Guadalupe Sabio, María López-Bravo, Carlos Ardavín

Correspondence

mlbravo@cnb.csic.es (M.L.-B.), ardavin@cnb.csic.es (C.A.)

In brief

Peritoneal immune cells reside unanchored within the peritoneal fluid in homeostasis. Vega-Pérez et al. reveal that large peritoneal macrophages drive the formation of mesothelium-bound, fibrin-dependent, multicellular aggregates, which enable peritoneal immune cells to control bacterial infection. Such resident macrophage aggregates may be central to antimicrobial immunity in other body cavities, such as the pleural cavity or brain ventricles.

Vega-Pérez et al., 2021, Immunity *54*, 2578–2594
November 9, 2021
https://doi.org/10.1016/j.immuni.2021.10.007

CellPress

CellPress

Immunity

Article

Resident macrophage-dependent immune cell scaffolds drive anti-bacterial defense in the peritoneal cavity

Adrián Vega-Pérez,[1,3] Laura H. Villarrubia,[1,3] Cristina Godio,[1] Alejandra Gutiérrez-González,[1] Lidia Feo-Lucas,[1] Margarita Ferriz,[1] Natalia Martínez-Puente,[1] Julieta Alcaín,[1,4] Alfonso Mora,[2] Guadalupe Sabio,[2] María López-Bravo,[1,*] and Carlos Ardavín[1,5,*]

[1]Departamento de Inmunología y Oncología, Centro Nacional de Biotecnología/CSIC, Darwin 3, 28049 Madrid, Spain
[2]Centro Nacional de Investigaciones Cardiovasculares, Melchor Fernández Almagro 3, 28029 Madrid, Spain
[3]These authors contributed equally
[4]Present address: Instituto de Medicina Experimental (CONICET), Buenos Aires, Argentina
[5]Lead contact
*Correspondence: mlbravo@cnb.csic.es (M.L.-B.), ardavin@cnb.csic.es (C.A.)
https://doi.org/10.1016/j.immuni.2021.10.007

SUMMARY

Peritoneal immune cells reside unanchored within the peritoneal fluid in homeostasis. Here, we examined the mechanisms that control bacterial infection in the peritoneum using a mouse model of abdominal sepsis following intraperitoneal *Escherichia coli* infection. Whole-mount immunofluorescence and confocal microscopy of the peritoneal wall and omentum revealed that large peritoneal macrophages (LPMs) rapidly cleared bacteria and adhered to the mesothelium, forming multilayered cellular aggregates composed by sequentially recruited LPMs, B1 cells, neutrophils, and monocyte-derived cells (moCs). The formation of resident macrophage aggregates (resMϕ-aggregates) required LPMs and thrombin-dependent fibrin polymerization. *E. coli* infection triggered LPM pyroptosis and release of inflammatory mediators. Resolution of these potentially inflammatory aggregates required LPM-mediated recruitment of moCs, which were essential for fibrinolysis-mediated resMϕ-aggregate disaggregation and the prevention of peritoneal overt inflammation. Thus, resMϕ-aggregates provide a physical scaffold that enables the efficient control of peritoneal infection, with implications for antimicrobial immunity in other body cavities, such as the pleural cavity or brain ventricles.

INTRODUCTION

Peritoneal bacterial infection can occur as the result of a pathological or traumatic loss of intestinal wall integrity, cirrhosis, abdominal surgery, or peritoneal dialysis. Unless locally controlled, infection spreads systemically and leads to sepsis (Angus and van der Poll, 2013). Abdominal, respiratory, and urinary tract bacterial infections are the main causes of sepsis (Vincent et al., 2009). During intraperitoneal (i.p.) bacterial infection, the release of proinflammatory mediators causes an overwhelming inflammatory reaction, leading to local peritoneal tissue injury and coagulation abnormalities that can provoke multisystemic acute organ dysfunction, and resulting in a life-threatening complex clinical syndrome called severe sepsis, which can ultimately lead to septic shock and death (Angus and van der Poll, 2013).

The mechanisms linking the exacerbated inflammation caused by abdominal infection to tissue damage, coagulopathy, and organ dysfunction have been extensively investigated. However, the mechanisms responsible for the control of i.p. bacterial infection in non-lethal sepsis, remain poorly understood. Resident F4/80$^+$ Tim4$^+$ peritoneal macrophages, called large peritoneal macrophages (LPMs, as opposed to F4/80$^-$ Tim4$^-$, monocyte-derived, small peritoneal macrophages, or SPMs) fulfill important functions in homeostasis (Bain and Jenkins, 2018), but their role against peritoneal infections is largely unexplored. Similarly, the contribution of SPMs in defense against infections remains unclear. Peritoneal mesothelial cells contribute to defense against microbial infection through the production of pro-inflammatory mediators that trigger the recruitment and activation of inflammatory cells (Mutsaers et al., 2015). During infection, neutrophils are recruited to the omentum through high endothelial venules located in milky spots and migrate to the peritoneal cavity, where they contribute to bacterial clearance (Buscher et al., 2016). Milky spots harbor a specialized vascular system and an organized lymphoid tissue supporting their potential role in antimicrobial immunity (Meza-Perez and Randall, 2017).

To explore the response of peritoneal immune cells to bacterial challenge and to understand how peritoneal immune cells, free in the peritoneal fluid in homeostasis, interact and fulfill their defense functions in the absence of a stromal support, we used

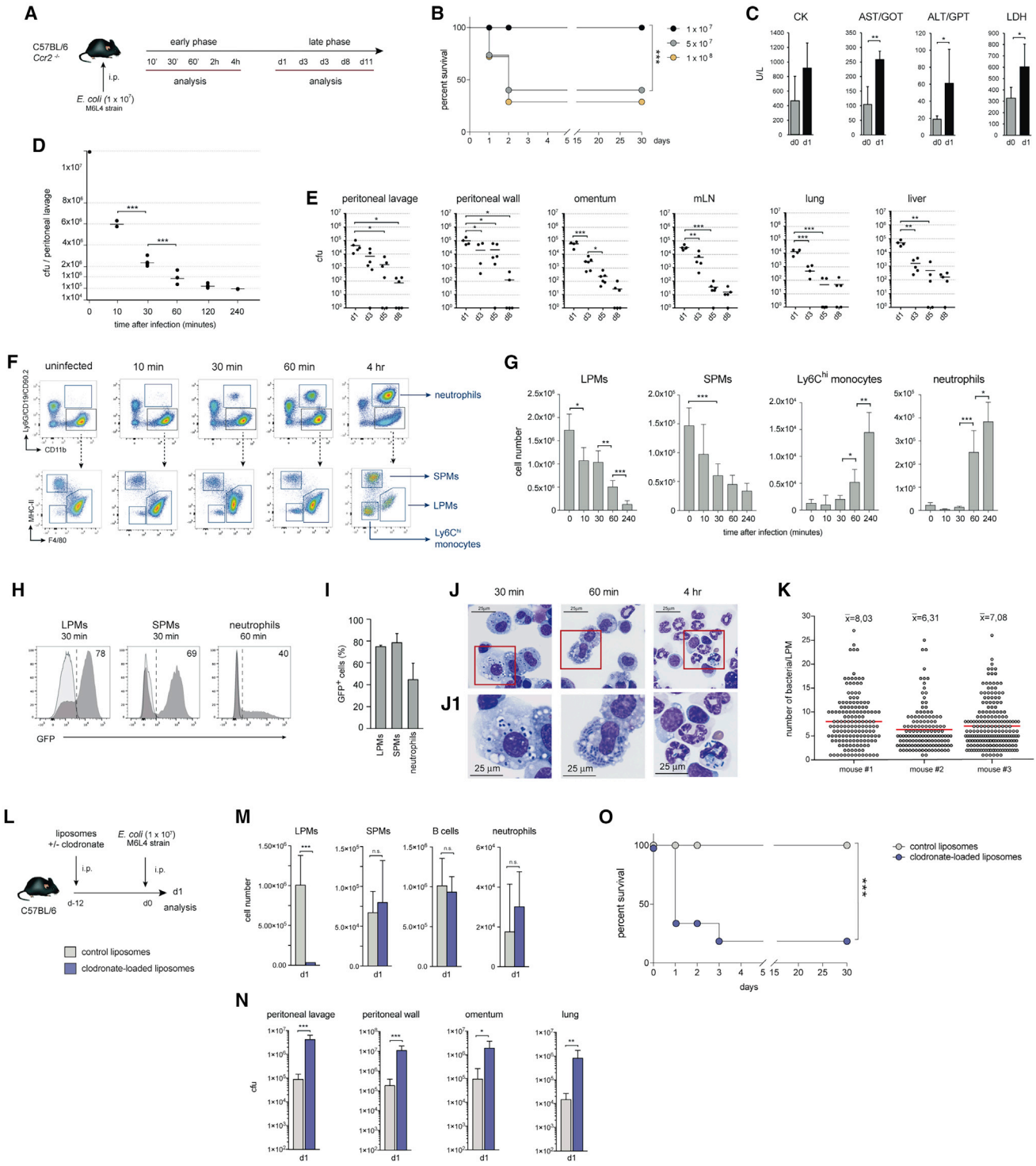

Figure 1. Bacterial clearance after i.p. *E. coli* infection is primarily achieved by LPMs

(A) *E. coli* infection protocol.

(B) Survival after *E. coli* infection at the indicated doses; n = 10.

(C) CK, AST/GOT, ALT/GPT, and LDH serum levels.

(D) Per-lavg bacterial load along the first 4 h.

(E) Bacterial load in per-lavg, per-wall, omentum, mediastinal lymph node (mLN), lung, and liver.

(F and G) FACS analysis and absolute number/mouse of LPMs, SPMs, monocytes, and neutrophils in the per-lavg.

(legend continued on next page)

an abdominal sepsis model based on the i.p. administration of a sublethal dose of *Escherichia coli*, a prevalent species in sepsis caused by Gram-negative bacteria (Opal et al., 2003). We found that LPMs fulfill an extensive bacterial elimination during the first hours after infection through the formation of mesothelial-bound multilayered cellular structures, or resMϕ-aggregates, which require a fibrin network and provide a dynamic physical scaffold for peritoneal immune cells. During the resolution of infection, LPMs controlled the recruitment of monocyte-derived cells (moCs) to resMϕ-aggregates; this was crucial for resMϕ-aggregate disruption by fibrinolysis and control of peritoneal overt inflammation. Thus, defense against peritoneal *E. coli* infection requires a complex interaction between coagulation, inflammation, and immunity largely controlled by LPMs and requiring the formation of dynamic immune scaffolds.

RESULTS

Bacterial clearance after i.p. *E. coli* infection is paralleled by the macrophage disappearance reaction (MDR)

We used an experimental model of abdominal sepsis relying on i.p. inoculum of *E. coli* M6L4 strain, in C57BL/6 (B6) mice (Figure 1A), at a 1×10^7 cfu sublethal dose, as defined in survival trials (Figure 1B). Analyses were performed during the early phase (hours) and late phase (days) of the response. Mice developed sepsis, as assessed by the increased serum levels of enzymes used to monitor liver, heart, and kidney damage (Figure 1C). The bacterial load in the peritoneal lavage (per-lavg) at 30 min was $\backsim 2 \times 10^6$ cfu and dropped to $\backsim 1 \times 10^5$ cfu at 4 h (Figure 1D). More than 95% of the bacteria were cleared during the first 24 h, and infection was resolved by the second week (Figure 1E).

Flow cytometry (fluorescence-activated cell sorting [FACS]) analysis of the peritoneal cavity revealed a strong reduction (up to 80%) in LPMs at 4 h (Figures 1F and 1G), a phenomenon classically described as MDR, paralleled by a reduction in SPMs and the recruitment of Ly6C^{hi} monocytes (hereafter, monocytes) and neutrophils (Figures 1F and 1G). Inoculation with GFP-labeled M6L4 *E. coli* (*E. coli*-GFP) revealed that at 30 min ~80% LPMs and 70% SPMs were GFP$^+$, and thus that $\sim 8 \times 10^5$ LPMs and 0.35×10^5 SPMs had internalized *E. coli* (Figures 1H and 1I). At 30 min, most LPMs had internalized bacteria, whereas at 60 min, only a minority contained bacteria (Figures 1J and 1J1). At 4 h, bacteria were hardly detectable and were mostly found in neutrophils. At 30 min, each LPM contained on average 7 bacteria (Figure 1K). Since $\sim 8 \times 10^5$ LPMs among those harvestable at 30 min had internalized *E. coli*, we estimated that these LPMs internalized at least 6×10^6 bacteria by 30 min postinfection (p.i.). At 60 min, neutrophils could be detected in the peritoneal cavity (Figure 1G), and ~40% were GFP$^+$ (Figures 1H and 1I), indicating that neutrophils contributed to bacterial uptake when LPMs had already carried out intensive bacteria internalization. Thus, LPMs fulfill efficient clearance of *E. coli* and are largely responsible for the reduction in bacterial load during the first hour p.i.

To further examine the functional relevance of LPMs during *E. coli* infection, we analyzed *LysM-Gata6*$^{-/-}$ mice in which LPMs display developmental and functional deficiencies (Gautier et al., 2014; Okabe and Medzhitov, 2014; Rosas et al., 2014). Although *LysM-Gata6*$^{-/-}$ mice displayed a 50% reduction in LPMs in steady state (Figure S1A), no differences in bacterial load were found when compared to wild-type (WT) mice (Figure S1B). Accordingly, *Gata6*$^{-/-}$ LPMs had a comparable ability to internalize *E. coli* (Figure S1C), supporting their microbicidal capacity. Nevertheless, since neutrophil recruitment was higher in *LysM-Gata6*$^{-/-}$ mice (Figure S1D), *E. coli* infection was analyzed after neutrophil depletion (Figure S1E) to assess whether neutrophils compensated the potential LPM defects in clearing *E. coli*. No differences in bacterial load were found between neutrophil-depleted, *LysM-Gata6*$^{-/-}$, and WT mice (Figure S1F), further supporting that *LysM-Gata6*$^{-/-}$ and WT mice were equally efficient in controlling *E. coli* infection.

These results led us to explore the role of LPMs during *E. coli* after LPM depletion by clodronate-loaded liposome (clodronate) treatment (Figure 1L). Mice were infected 12 days after LPM depletion to ensure that potential inflammatory reaction to liposome treatment was resolved (Figure 1M). LPM depletion led to an almost 2-log increase in the bacterial load (Figure 1N) and to an increase in mortality rate (Figure 1O), revealing a crucial role for LPMs in the control of *E. coli* infection.

LPMs promote the formation of mesothelium-bound resMϕ-aggregates during i.p. *E. coli* infection

The intensive internalization of bacteria by LPMs was followed by the MDR, which may reflect that LPMs were no longer retrievable because they adhered to mesothelial cells lining the peritoneal cavity, as proposed in different MDR models (Barth et al., 1995). The analysis of the inner face of the peritoneal wall (per-wall) by whole-mount immunofluorescence (WMI) and confocal microscopy (CF), revealed that aggregates of F4/80^{bright} resident macrophages (hereafter resMϕ-aggregates) were found in the per-wall at 4 h, ranging from small to large (>800 μm) and densely packed aggregates (Figures 2A, 2B, and S1G); macrophages were also found spread over the mesothelium (Figure 2A1). ResMϕ-aggregates were detectable from 30 min and lay over

(H and I) FACS analysis and quantification of *E. coli*-GFP internalization; (H) light profiles: background staining; the percentage of GFP$^+$ cells is indicated.
(J and J1) Per-lavg cytospin preparations; Giemsa staining.
(K) Number of bacteria/LPM estimated in 9 micrographs/mouse at 30 min. The mean number of bacteria/LPM is indicated; each dot corresponds to an individual cell.
(L) LPM depletion and *E. coli* infection protocol.
(M) LPM, SPM, B cell, and neutrophils absolute number/mouse in per-lavg at d1 in control or clodronate-treated mice.
(N) Bacterial load in per-lavg, per-wall, omentum, and lung at d1 in control or clodronate-treated mice.
(O) Survival of control or clodronate-treated mice after *E. coli* infection; n = 10. Data expressed as means ± SDs of 5 mice/condition. Similar results were obtained in at least 3 independent experiments. *, $p < 0.05$; **, $p < 0.01$; ***, $p < 0.001$
See also Figure S1.

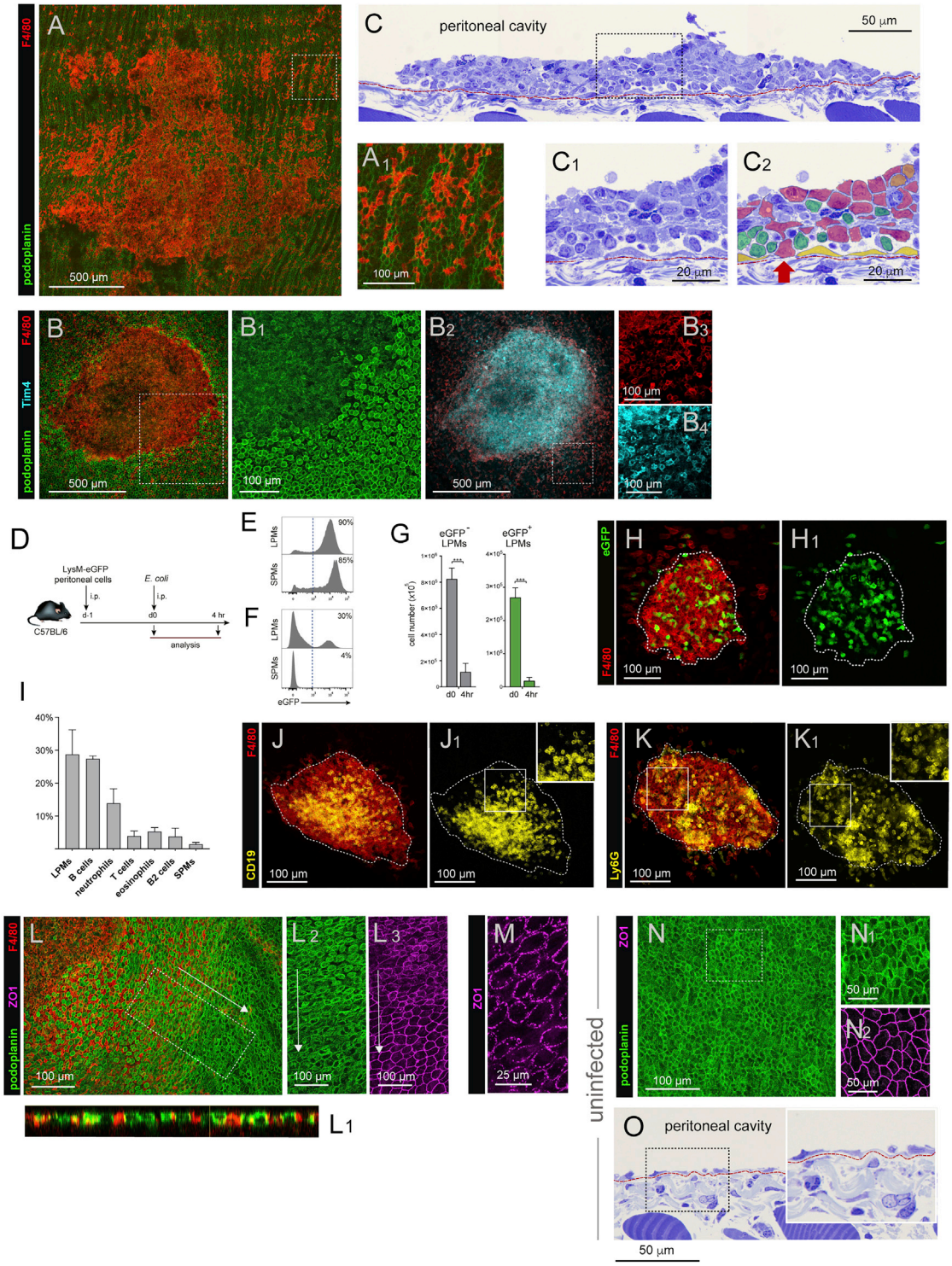

Figure 2. Peritoneal *E. coli* infection promotes the formation of resMϕ-aggregates attached to the mesothelium

(A) WMI + CF of per-wall at 4 h.

(A1) Enlargement of (A).

(B) WMI+CF of a resMϕ-aggregate in per-wall at 24 h.

(B1) Enlargement of (B).

(B2) Tim4/F4/80 staining of the area shown in (B).

(B3 and B4) Enlargement of (B2).

(legend continued on next page)

the mesothelium, as assessed by podoplanin staining (Figures 2B and 2B1), light microscopy, and electron microscopy (Figures 2C1, 2C2, and S2A).

ResMϕ-aggregates were not detectable in uninfected mice, suggesting that the F4/80^{bright} resident macrophages forming them were LPMs no longer harvestable by per-lavg; accordingly, F4/80^{bright} macrophages expressed the LPM marker Tim4 (Figures 2B2–2B4). To confirm this hypothesis, peritoneal cells from LysM-EGFP mice, in which EGFP is expressed by myeloid cells, were transferred into B6 mice, infected 24 h later (Figure 2D). Peritoneal EGFP$^+$ cells of LysM-EGFP mice made up >85% of LPMs and SPMs (Figure 2E). At day 0 (d0), transferred EGFP$^+$ LPMs accounted for ~30% of total LPMs, whereas no EGFP$^+$ SPMs were detectable (Figure 2F), reflecting their high turnover (Bain et al., 2016). Transferred EGFP$^+$ LPMs and endogenous EGFP$^-$ LPMs underwent a comparable MDR (Figure 2G); in addition, EGFP$^+$ LPMs were found within the resMϕ-aggregates (Figure 2H), supporting the notion that macrophages forming resMϕ-aggregates were LPMs.

ResMϕ-aggregates were heterogeneous, multi-layered structures, composed predominantly by macrophages, but also by lymphoid cells, neutrophils, eosinophils, and mast cells (Figures 2C, 2C1, 2C2 and S2A–S2C). Most macrophages displayed numerous filopodia (Figure S2B), suggesting high motility. Analysis of disaggregated resMϕ-aggregates indicated that macrophages, B1-cells, and neutrophils made up to 90% of resMϕ-aggregates (Figure 2I). This was confirmed on WMI preparations by F4/80, CD19, and Ly6G staining, revealing that B1 cells were mainly located in the center of resMϕ-aggregates (Figures 2J, 2J1, 2K, and 2K1). Since LPMs, B1 cells, and neutrophils were the main components of resMϕ-aggregates, we assessed whether resMϕ-aggregate formation required these cells. ResMϕ-aggregates were not detectable after *E. coli* infection in LPM-depleted mice. Xid mice carrying a point mutation in Bruton's tyrosine kinase, which leads to a severe deficiency in B1 cell development (Khan et al., 1995), displayed a strong reduction in peritoneal B cells at 4 h (Figure S1H), but underwent an MDR (Figure S1I) and formed resMϕ-aggregates comparable to WT mice. Similarly, neutrophil-depleted mice (Figure S1J) that displayed a strong reduction in peritoneal neutrophils at 4 h (Figure S1K) underwent MDR (Figure S1L) and formed resMϕ-aggregates comparable to control mice. The formation of resident macrophage aggregates therefore required LPMs, but this can occur in the absence of B1 cells or neutrophils.

The mesothelium located beneath and surrounding resMϕ-aggregates (Figures 2B1, 2L, and 2L1) lost the pavement-like organization found in areas distant from resMϕ-aggregates (Figures 2L and 2L1–2L2) and in uninfected mice (Figures 2N, 2N1, and 2O). CF (Figures 2B1 and 2L1) and electron microscopy (Figure S2C) revealed the existence of gaps in the mesothelium, so that macrophages surrounding the aggregates were found between mesothelial cells (Figures 2L and 2L1). Accordingly, the tight junction pattern of mesothelial cells, identifiable by the tight junction protein ZO1, found in areas distant from resMϕ-aggregates and in uninfected mice (Figures 2L3, 2M, and 2N2), was markedly disrupted in mesothelial cells associated with resMϕ-aggregates.

To extend these observations to a polymicrobial abdominal sepsis model, we used the cecal slurry injection (CSI) method. At 4 h after CSI, resMϕ-aggregates were detected in the per-wall (Figures S1M–S1M3) and omentum (Figures S1N–S1N3). CSI and i.p. *E. coli* infection promoted comparable MDR and neutrophil recruitment kinetics (Figure S1O).

Fibrin-dependent resMϕ-aggregates control i.p. *E. coli* infection and prevent its spread to the periphery

Pioneer studies proposed that the MDR was caused by the attachment of macrophages to the peritoneal mesothelium and could be partially reverted by heparin (Barth et al., 1995), suggesting that MDR may involve fibrin formation. We thus explored whether resMϕ-aggregates involved fibrin polymerization. Fibrinogen staining confirmed the presence of a fibrin network between cells forming resMϕ-aggregates and extending to the surrounding mesothelial cells (Figures 3A–3A2); ~100-nm-thick fibrin fibers in close contact with macrophages were detectable by electron microscopy (Figures 3B–3B2). The functional relevance of resMϕ-aggregates after *E. coli* infection was addressed by preventing their formation through the inhibition of fibrin polymerization. Mice were treated i.p. with heparin and infected with *E. coli* (Figure 3C). Only a low number of small macrophage

(C) Per-wall semi-thin section at 4 h showing a resMϕ-aggregate; red line: mesothelial basal membrane.
(C1 and C2) Enlargement of C. In C2: macrophages: red; lymphocytes: green; mesothelial cells: yellow. Arrow: mesothelial discontinuity.
(D) LysM-eGFP peritoneal cell transfer and *E. coli* infection protocol.
(E) eGFP expression by LPMs and SPMs in non-infected LysM-eGFP mice; the percentage of eGFP$^+$ cells is indicated.
(F) eGFP expression by LPMs and SPMs in B6 mice after transfer of LysM-eGFP peritoneal cells; the percentage of eGFP$^+$ cells is indicated.
(G) Absolute number/mouse of GFP$^-$ and GFP$^+$ LPMs in B6 mice after transfer of LysM-eGFP peritoneal cells at d0 and 4 h.
(H and H1) WMI + CF of a resident macrophage-aggregate after transfer LysM-eGFP peritoneal cells at 4 h.
(I) Relative proportion of the cell types present in resMϕ-aggregates at 4 h; FACS analysis.
(J–K1) WMI + CF of resMϕ-aggregates at 4 h.
(J and J1) F4/80/CD19 staining.
(K and K1) F4/80/Ly6G staining.
(L) Per-wall WMI + CF at 24 h.
(L1) Orthogonal view of the area defined in (L).
(L2 and L3) Enlargement of (L).
(M) High-resolution micrograph of an area similar to (L3).
(N–N2) Per-wall WMI + CF of a non-infected mouse.
(O) Semi-thin section of a non-infected per-wall. Red line: mesothelial basal membrane.
Dashed line in (H), (J), and (K) ResMϕ-aggregate limits. Data expressed as means ± SDs of 5 mice/condition. Similar results were obtained in at least 3 independent experiments. ***, $p < 0.001$
See also Figures S1 and S2.

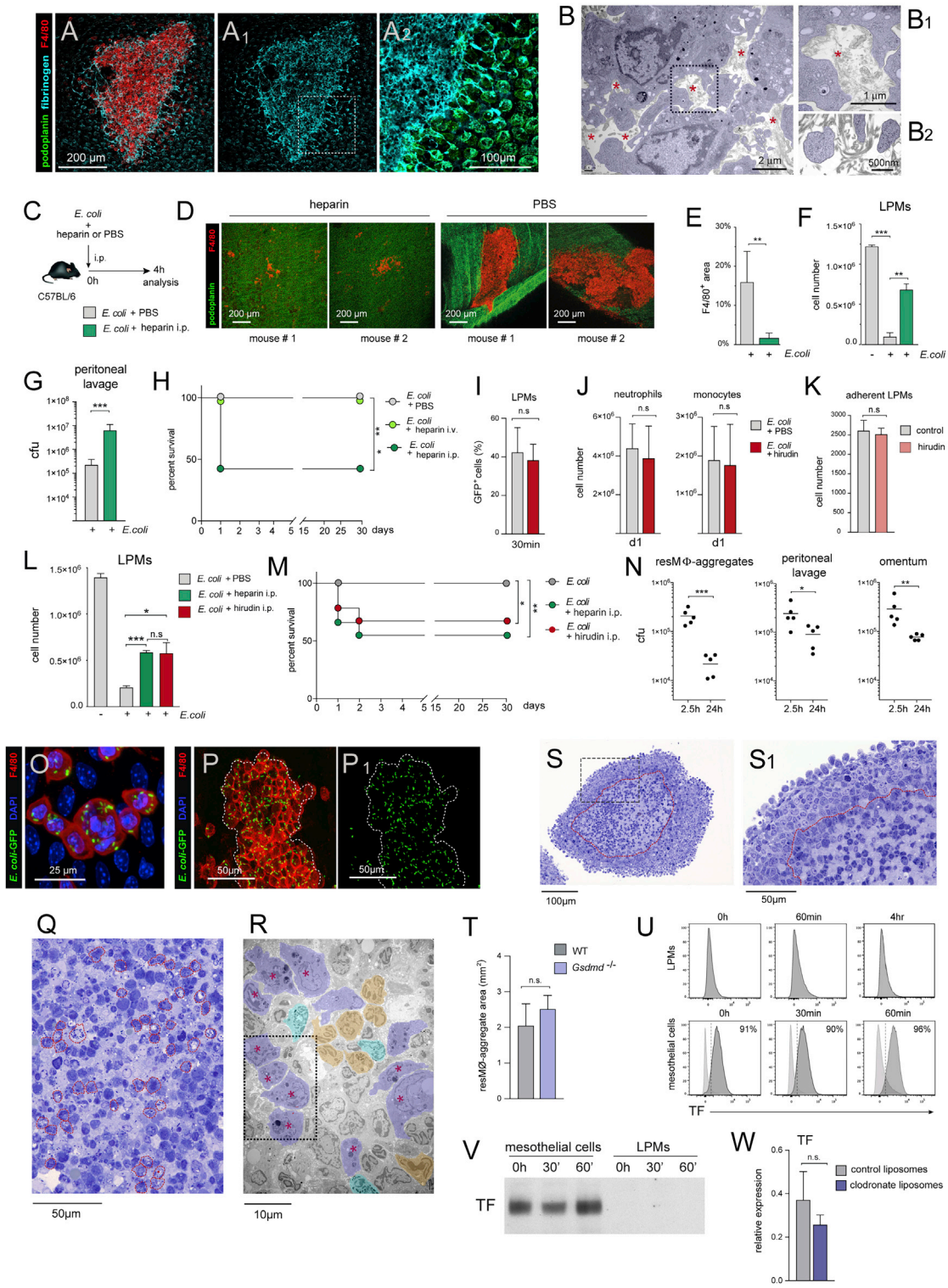

Figure 3. Fibrin-dependent resMϕ-aggregate formation is crucial for controlling i.p. *E. coli* infection

(A and A1) Per-wall WMI + CF at 4 h.

(A2) Enlargement of (A1).

(B and B1) Electron microscopy of a resMϕ-aggregate at 4 h. Fibrin fibers (asterisks) in close contact with macrophages (violet).

(B2) High-magnification electron microscopy image of a resMϕ-aggregate at 4 h, showing fibrin fibers with a ~100-nm diameter in close contact with macrophages (violet).

(legend continued on next page)

aggregates were detectable in heparin-treated mice (Figures 3D and 3E). Accordingly, ~50% LPMs were harvestable at 4 h in heparin-treated mice versus <10% in control mice (Figure 3F). Interestingly, a 2-log increase in bacterial load was found in heparin-treated mice (Figure 3G), paralleling a dramatically increased mortality rate (Figure 3H).

To exclude that the higher mortality associated with i.p. heparin treatment was due to the inhibition of microvascular thrombus or extracellular traps that may compromise peripheral bacterial clearance, and not to the blockade of resMϕ-aggregate formation, mice were treated with heparin intravenously (i.v.). Under these conditions, resMϕ-aggregates formed, and survival was not compromised (Figure 3H), supporting that the lower survival of mice treated with heparin i.p. was related to the prevention of resMϕ-aggregate formation. Since heparin could interfere with processes not involving fibrin, including cell adhesion and migration (Lever and Page, 2002), it is conceivable that their inhibition by heparin may contribute to the higher susceptibility to the infection of mice treated with heparin i.p. Thus, to ascertain the effect of blocking resMϕ-aggregate formation, mice were treated with hirudin, a specific thrombin inhibitor that prevents fibrin formation, but is not expected to interfere with fibrin-independent processes that could be inhibited by heparin. Hirudin did not affect *in vivo E. coli* internalization by LPMs, nor the *E. coli*-induced neutrophil and monocyte recruitment to the peritoneal cavity (Figures 3I and 3J). LPM adherence to plastic was not affected by hirudin (Figure 3K). Interestingly, LPMs retrievable at 4 h and survival were comparable in mice treated i.p. with hirudin or heparin (Figures 3L and 3M). These data confirm that resMϕ-aggregate formation was dependent on thrombin-mediated fibrin polymerization, and that resMϕ-aggregates fulfilled an essential function in the control of infection. Accordingly, the reduction in bacterial load from 2.5 to 24 h was higher in resMϕ-aggregates than in the per-lavg and omentum (Figure 3N).

LPMs forming resMϕ-aggregates contained bacteria and bacteria were not found outside resMϕ-aggregates (Figures 3O–3P1). Numerous macrophages containing degraded bacteria were found particularly in the central area of resMϕ-aggregates (Figures 3Q, 3R, and S2D), which also harbored necrotic macrophages and neutrophils that internalized bacteria (Figures 3S, 3S1, S2E, and S2F). The periphery of resMϕ-aggregates contained macrophages and neutrophils not containing bacteria, suggesting that they have adhered later to resMϕ-aggregates, initially formed by LPMs that internalized bacteria.

The formation of resMϕ-aggregates required thrombin-dependent fibrin polymerization and therefore the activation of coagulation. Since tissue factor (TF) plays an essential role in coagulation in mouse models of sepsis (Gando et al., 2016; Grover and Mackman, 2018), we hypothesized that TF triggered the coagulation process leading to the fibrin network in resMϕ-aggregates. Systemic coagulation was induced by TF-containing microvesicles released by pyroptotic monocytes after inflammasome activation (Wu et al., 2019). However, TF production by pyroptotic cells did not appear to trigger fibrin polymerization after i.p. *E. coli* infection since resMϕ-aggregate formation was unaffected in *Gsdmd*$^{-/-}$ mice (Figure 3T), in which pyroptosis-induced coagulation is defective (Wu et al., 2019). Moreover, although LPMs were reported to express TF after *in vivo* LPS stimulation (Ahamed et al., 2007), TF was not detectable in LPMs after *E. coli* infection (Figures 3U and 3V). TF was expressed by mesothelial cells before and after infection, supporting that they were the primary source of TF in the peritoneal cavity after *E. coli* infection (Figures 3U and 3V). Accordingly, no difference was detectable in the concentration of TF in the per-lavg between control and LPM-depleted mice (Figure 3W).

(C) Heparin i.p. treatment and *E. coli* infection protocol.
(D) Per-wall WMI + CF of i.p. heparin- and PBS-treated mice at 4 h.
(E) Area occupied by resMϕ-aggregates at 4 h in PBS- and i.p. heparin-treated mice; mean percentage of F4/80 staining/micrograph ± SDs of 4 micrographs/condition.
(F) LPM absolute number in per-lavg of uninfected and PBS- and i.p. heparin-treated mice at 4 h.
(G) Per-lavg bacterial load of PBS- and i.p. heparin-treated mice at 4 h.
(H) Survival after *E. coli* infection of PBS-, intraperitoneally (i.p.), and intravenously (i.v.) heparin-treated mice; n = 10.
(I) *E. coli*-GFP internalization by LPMs in PBS- and i.p. hirudin-treated mice at 30 min.
(J) Absolute number/mouse of neutrophils and monocytes in the per-lavg of PBS- and i.p. hirudin-treated mice at d1.
(K) Quantification of LPM adherence to plastic in the absence or presence of 100 μg/mL huridin; mean number of adherent LPMs/micrograph ± SDs of 4 micrographs/condition.
(L) LPM absolute number/mouse in the per-lavg of uninfected, and untreated, i.p. heparin-treated, and i.p. hirudin-treated mice at 4 h.
(M) Survival after *E. coli* infection of PBS-, i.p. heparin-treated, and i.p. hirudin-treated mice; n = 10.
(N) Bacterial load in resMϕ-aggregates, per-lavg, and omentum at 2.5 and 4 h.
(O) High magnification WMI + CF image of a resMϕ-aggregate at 2 h showing *E. coli*-GFP internalized by LPMs.
(P and P1) WMI + CF of a resMϕ-aggregate at 2 h p.i. with *E. coli*-GFP. Dashed line: resident macrophage aggregate limit.
(Q) Semi-thin section of a resMϕ-aggregate at 4 h; cells containing bacteria are marked with a red dashed line.
(R) Electron microscopy of a resMϕ-aggregate at 4 h. Macrophages (violet) with degraded bacteria (asterisks); neutrophils: orange; eosinophils: turquoise.
(S and S1) Semi-thin section of a resMϕ-aggregate at 4 h; dashed line: limits of central area harboring necrotic macrophages and neutrophils.
(T) Quantification of the resMϕ-aggregate area/mouse after strong per-lavg, in WT and *Gsdmd*$^{-/-}$ mice, at 2 h, performed as shown in Figures 7G and 7H; mean resMϕ-aggregate area/micrograph ± SDs of 4 micrographs/condition.
(U) FACS analysis of TF expression by LPMs and mesothelial cells. Mesothelial cells were analyzed after gating for CD45^{-} ICAM-1^{+} cells. Light gray profiles: isotype control staining; the percentage of TF^{+} cells is indicated.
(V) WB analysis of TF expression by mesothelial cells and LPMs.
(W) Quantification of TF in the peritoneal cavity of control or clodronate-treated mice at 4 h using the Proteome profiler mouse XL cytokine array; n = 2. Data expressed as means ± SDs of 5 mice/condition. Similar results were obtained in at least 3 independent experiments. *, $p < 0.05$; **, $p < 0.01$; ***, $p < 0.001$
See also Figure S2.

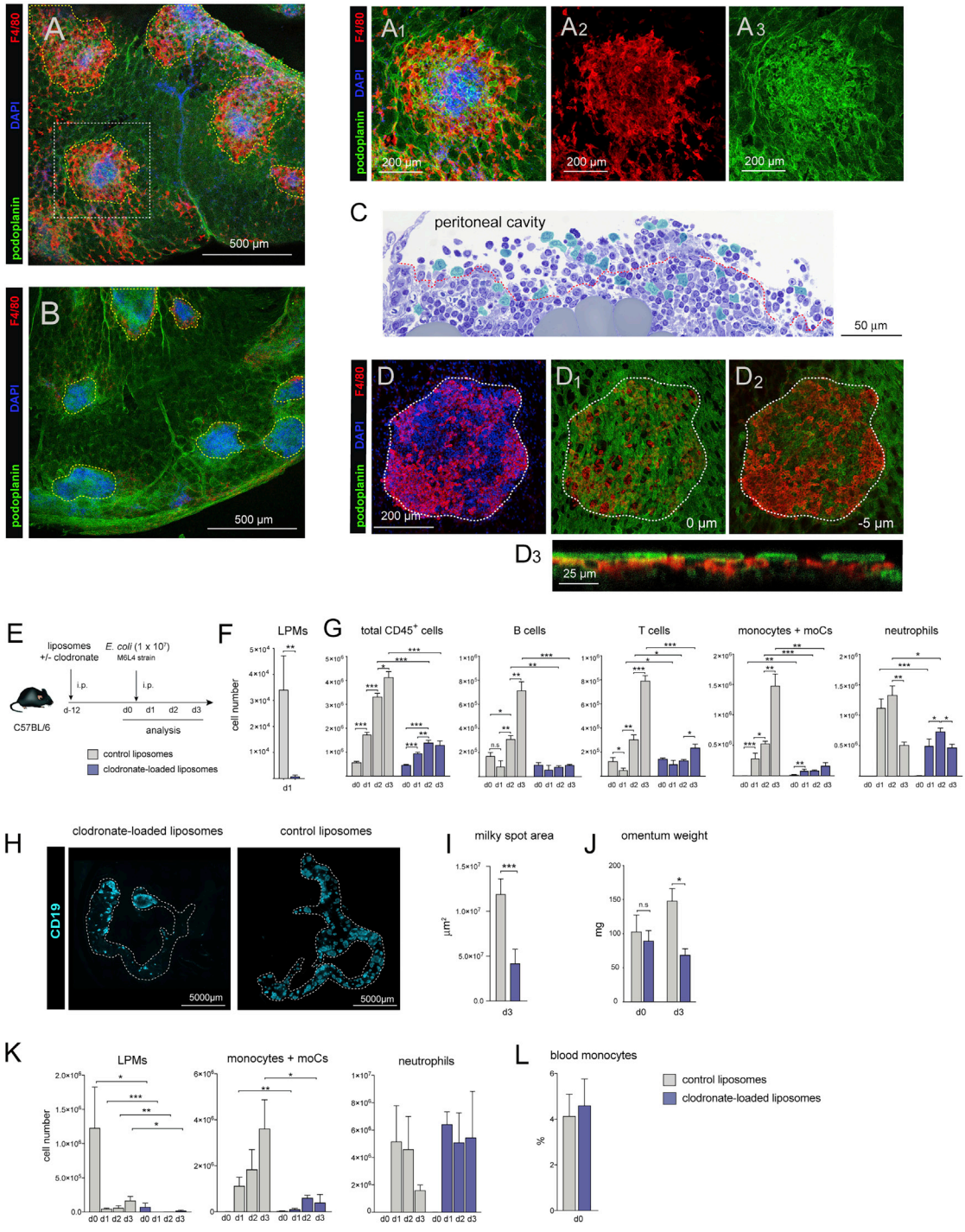

Figure 4. LPMs accumulate in the omentum and promote milky spot development after *E. coli* infection

(A) WMI + CF of the omentum at 4 h; yellow dashed lines: milky spots.

(A1–A3) Enlargement of the white square area in (A) showing a milky spot-associated macrophage aggregate.

(B) WMI + CF of a non-infected omentum. Yellow dashed lines: milky spots.

(C) Omentum semi-thin section at 4 h showing macrophages (turquoise) infiltrating a milky spot; dashed line: mesothelial lining.

(D–D2) WMI + CF of a milky spot-associated macrophage aggregate at 4 h.

(D1 and D2) CF images obtained at the mesothelial level (D1) and 5 µm underneath (D2). White line: macrophage aggregate limits.

(D3) Orthogonal view of the aggregate shown in (D).

(E) Protocol of omentum analysis after LPM depletion and *E. coli* infection.

(legend continued on next page)

LPMs accumulate in the omentum and promote milky spot development during *E. coli* infection

Aggregates of F4/80^{bright} macrophages were found to be associated with the omental milky spots at 4 h (Figures 4A–4A3), but not in uninfected mice (Figure 4B). F4/80^{bright} macrophages infiltrated the milky spots through the discontinuities of the mesothelium, which appeared particularly disorganized as demonstrated in semi-thin sections (Figure 4C), CF images obtained at different heights along the z axis (Figures 4D–4D2) and orthogonal views (Figure 4D3). The majority of cells forming milky spot-associated aggregates were F4/80^{bright} Tim4^{+} macrophages and a lower proportion of neutrophils; a minor population of F4/80^{dim} Tim4^{+} macrophages was detectable (Figures S3A, S3A1, and S3B). In addition to milky spot-associated macrophage aggregates, compact F4/80^{bright} Tim4^{+} macrophage aggregates, comparable to per-wall resMϕ-aggregates, were located in milky spot-devoid zones (Figures S3D, S3D1, and S3C). The latter lay over the mesothelium (Figures S3C and S3D2) and displayed a developed fibrin network (Figures S3E and S3E1).

To explore whether Tim4^{+} F4/80^{hi} macrophages forming aggregates in the omentum were LPMs, we assessed whether LPMs migrated to the omentum by labeling peritoneal cavity cells *in vivo* before *E. coli* infection (Figure S3F). Carboxyfluorescein succinimidyl ester (CFSE)-labeled F4/80^{hi} macrophages, expressing Tim4 and Gata6, were detectable in the omentum at d1 (Figure S3G). These cells corresponded to LPMs as they were not detectable in uninfected mice, and no CFSE labeling was detectable in the omentum before infection (Figure S3H). To confirm that these LPMs corresponded to F4/80^{bright} Tim4^{+} macrophages forming omental macrophage aggregates, peritoneal cells from LysM-EGFP mice were transferred into B6 mice before infection (Figure S3I). EGFP^{+} F4/80^{bright} Tim4^{+} macrophages found in omental macrophage aggregates at 4 h (Figures S3J–S3J2) corresponded to LPMs, since only LPMs expressed EGFP after transfer of LysM-EGFP cells (Figure 2F). EGFP^{+} macrophages detectable at 4 h had a F4/80^{hi} major histocompatibility complex class II^{lo} (MHC-class II^{lo}) phenotype (Figure S3K) similar to endogenous LPMs migrating to the omentum after infection (Figure S3G). *E. coli* infection thus promoted the migration of LPMs to the omentum, resulting in the formation of mesothelium-bound LPM aggregates and milky spot-associated LPM aggregates. Heparin treatment caused an 85% reduction in omental LPMs (Figure S3L) and blocked the formation of mesothelium-bound and milky spot-associated LPM aggregates (Figures S3M and S3N). In contrast, hirudin treatment led to a 50% LPM reduction and prevented the formation of mesothelium-bound but not of milky spot-associated LPM aggregates (Figure S3O), supporting that the former required the formation of a thrombin-dependent fibrin network, not required for LPM aggregation in milky spots. Accordingly, a dense fibrin network was detectable in mesothelium-bound aggregates in untreated mice (Figures S3M1 and S3M2), but not in heparin- or hirudin-treated mice (Figures S3N1, S3N2, and S3O1-S3O2).

Zymosan stimulation increases omental milky spots and fat-associated lymphoid clusters (FALCs) present in the mesentery and gonadal fat (Bénézech et al., 2015). This led us to investigate whether LPM migration to the omentum promoted leukocyte recruitment to milky spots during *E. coli* infection (Figures 4E and 4F). In control mice, *E. coli* infection increases B cells, T cells, monocytes, moCs (defined as CD11b^{+} MHC-class II^{+} Ly6C^{int}) and neutrophil recruitment to milky spots (Figure 4G). In contrast, in LPM-depleted mice, the recruitment to the omentum of B cells, T cells, monocytes, and, to a lesser extent, neutrophils, was impaired (Figure 4G), and the milky spot area (Figures 4H and 4I) and omentum weight (Figure 4J) were reduced. In addition, LPMs controlled the recruitment of inflammatory cell subsets to the peritoneal cavity, since monocyte and moC recruitment was impaired in LPM-depleted mice, while neither neutrophil recruitment nor circulating monocytes were unaffected by LPM depletion (Figures 4K and 4L). Thus, leukocyte recruitment to the omentum and monocyte and moC recruitment to the peritoneal cavity after *E. coli* infection was dependent on LPMs.

F4/80^{bright} Tim4^{+} macrophage aggregates, comparable to those formed in the omentum, were found in the mesentery (Figures S3P–S3P3) and gonadal fat (Figures S3Q–S3Q3), associated with the FALCs, that harbor an organized lymphoid tissue and a specialized vascular system comparable to those of the omentum. This supports that resMϕ-aggregates are predominantly formed anchored to the mesothelium lining peritoneal adipose tissue-containing organs and the peritoneal wall.

E. coli infection leads to LPM death by pyroptosis

After blocking resMϕ-aggregate formation, only ~40%–50% of LPMs can be retrieved by per-lavg (Figure 3I), suggesting that *E. coli* infection caused the death of a fraction of LPMs. At 30 min, virtually the entire LPM population was harvestable by per-lavg (Figure 5A), but ~40% LPMs were annexin-V^{+} 7-AAD^{+} (Figure 5B), indicating that they underwent a non-apoptotic cell death. Accordingly, LPMs displaying nuclear and cytoplasmic swelling characteristic of necrotic cell death were detectable at 30 min (Figures 5C–5C1), but not in uninfected mice (Figures 5D–5D1). LPM death did not correlate with bacterial uptake since the percentage of dead cells was comparable within LPMs that had or had not internalized bacteria (Figures 5E and 5F).

(F) LPM absolute number/mouse LPMs at d1 in the omentum in control or clodronate-treated mice.
(G) Absolute number/mouse of the indicated subsets in the omentum in control or clodronate-treated mice.
(H) WMI + CF image of the whole omentum in control or clodronate-treated mice at d3; dashed lines: limits of the omentum.
(I) Quantification of milky spot area (identified by CD19 staining as shown in H) in control or clodronate-treated mice at d3; mean CD19^{+} area/micrograph ± SDs of 4 images/condition.
(J) Omentum weight in control or clodronate-treated mice at d0 and d3.
(K) Absolute number/mouse of total LPMs, monocytes, and neutrophils in the per-lavg of control or clodronate-treated mice.
(L) Absolute number/mouse of blood monocytes from uninfected mice at d12 after clodronate treatment. Data expressed as means ± SDs of 5 mice/condition. Similar results were obtained in 2–3 independent experiments. *, $p < 0.05$; **, $p < 0.01$; ***, $p < 0.001$
See also Figure S3.

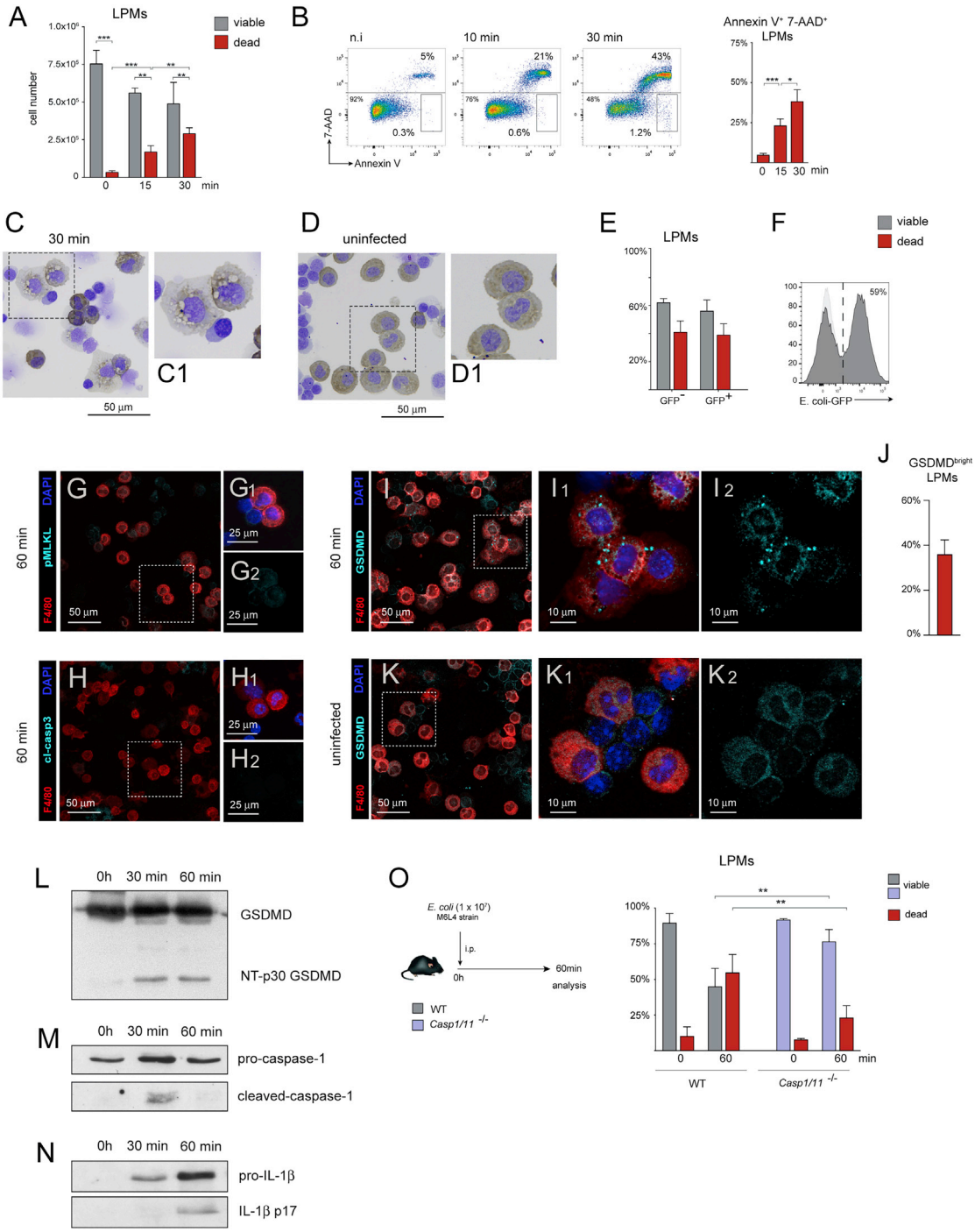

Figure 5. *E. coli* infection leads to LPM death by pyroptosis

(A) Absolute number/mouse of viable and dead (7-AAD$^+$) LPMs in per-lavg.

(B) FACS analysis and quantification of annexin-V$^+$ 7-AAD$^+$ LPMs in per-lavg.

(C–D1) Per-lavg cytospin preparations at 30 min showing necrotic F4/80$^+$ LPMs (C) and LPMs in an uninfected mouse (D); F4/80 peroxidase/toluidine blue staining.

(E) Relative proportion of viable and dead cells among LPMs that had and had not internalized *E. coli*-GFP at 60 min, defined by their GFP expression, as shown in (F).

(F) GFP expression by LPMs at 60 min p.i. with *E. coli*-GFP; the percentage of GFP$^+$ LPMs is indicated.

(G–I) Detection of pMLKL (G), cleaved caspase-3 (cl-casp3) (H), and GSDMD (I) by CF in per-lavg cytospin preparations at 60 min.

(G1 and G2) F4/80/DAPI (G1) and pMLKL (G2) staining.

(H1 and H2) F4/80/DAPI (H1) and cl-casp3 (H2) staining.

(legend continued on next page)

LPMs expressing phospho-mixed lineage kinase domain-like (MLKL) or cleaved caspase-3 were not detectable at 60 min (Figures 5G–5G2 and 5H–5H2), suggesting that neither necroptosis nor apoptosis caused LPM death. Interestingly, at 60 min ~40% LPMs displayed a gasdermin (GSDMD) staining correlating with pore formation (Figures 5I–5I2 and 5J) resulting from GSDMD oligomerization (Rathkey et al., 2017), whereas LPMs from uninfected mice displayed a diffuse GSDMD staining, reflecting its non-pore-forming state (Figure 5K–5K2), supporting that *E. coli* infection led to LPM pyroptosis. Pore formation depends on GSDMD cleavage, commonly by caspase-1 or caspase-11, generating the N-terminal p30 GSDMD fragment (NT-p30 GSDMD). Active caspase-1 also mediates the cleavage of pro-interleukin-1β (IL-1β) and pro-IL-18 (Jorgensen et al., 2017). GSDMD cleavage and NT-p30 GSDMD were detected by western blot in LPMs at 30 and 60 min (Figure 5L); accordingly, cleaved caspase-1 was detected at 30 min (Figure 5M), confirming that LPMs were undergoing pyroptosis. *E. coli* infection triggered the synthesis of pro-IL-1β, detectable at 30 min, that was subsequently cleaved into its mature form, IL-1β p17, detectable at 60 min (Figure 5N). *Casp1/11*$^{-/-}$ mice displayed a reduction in dead LPMs at 60 min (Figure 5O), further supporting that *E. coli* infection caused LPM pyroptosis, leading to the release of proinflammatory cytokines and peritoneal inflammation.

Kinetics of LPMs during the resolution of *E. coli* infection

Since *E. coli* infection caused the death of a high proportion of LPMs, we sought to analyze the fate of the LPM population during the resolution of infection. At d1, a low number of viable LPMs was detectable, but their number increased from d3 and reached ~70% of the number in uninfected mice by d8–d11 (Figure 6A), when low levels of bacterial load (Figure 1E) and neutrophils (Figure 6A) were detectable. Tim4 and Gata6 expression was comparable in control and d11 LPMs (Figure 6B). Most LPMs present at d8 corresponded to or derived from those present before infection, as assessed by *in vivo* labeling of peritoneal cells (Figure 6C), which revealed that >90% LPMs remained labeled at d8 (Figures 6D and 6E). Most SPMs and T cells were replaced at d1 and >80% B cells were replaced at d8. Neither neutrophils nor the majority of monocytes recruited at d1 were labeled (Figure 6F). As a high proportion of LPMs died along the first hours, LPMs had to proliferate to reach their number at d8 (Figure 6A). Accordingly, Far-Red dilution occurred in LPMs from d1 to d8 (Figure 6D) and LPM proliferation increased from d0 to d5 (Figure 6G). Thus, LPMs that died along the early phase of infection were largely replaced by the proliferation of the initial LPM population.

moCs control fibrinolysis-dependent resMϕ-aggregate disruption and prevent peritoneal overt inflammation

We next analyzed the evolution of resMϕ-aggregates during the resolution of infection, since after these structures had fulfilled their bacterial containment and elimination function, dead cells within need to be eliminated and fibrin degraded to dampen its proinflammatory potential. At d4, aggregates were composed predominantly of Tim4^{-} macrophages with a lower F4/80 expression than LPMs (F4/80^{int} Tim4^{-} macrophages) and a reduced number of F4/80^{bright} Tim4^{+} LPMs (Figures 7A–7A3). LPMs were mainly located in the central part interspersed among mesothelial cells that appeared markedly disorganized, displaying wide gaps and a disrupted tight junction pattern (Figures 7A4 and 7B–7D). LPMs were located between mesothelial cells or in the submesothelial space (Figure 7B), whereas F4/80^{int} Tim4^{-} macrophages were found in the submesothelial space (Figure 7C). Since F4/80^{int} Tim4^{-} macrophages present in d4 aggregates were not detectable in resMϕ-aggregates at 4 h, we hypothesized that they derive from inflammatory monocytes. Accordingly, in CCR2-deficient mice (*Ccr2*$^{-/-}$ mice), in which monocyte egress from the bone marrow and recruitment to inflammatory foci are impaired (Shi and Pamer, 2011), F4/80^{int} Tim4^{-} macrophagewere almost undetectable in d4 aggregates. These contained mainly F4/80^{bright} Tim4^{+} LPMs (Figures 7E–7E3) and did not exhibit the profound mesothelial alterations of WT mice (Figure 7E4), supporting that F4/80^{int} Tim4^{-} macrophages derived from monocytes. Consistently, infiltrating moCs (defined as shown in Figure S4A) increased progressively during infection in WT mice, but were reduced in *Ccr2*$^{-/-}$ mice (Figure 7F). Accordingly, monocytes were actively recruited to the per-wall in WT, but not in *Ccr2*$^{-/-}$ mice (Figure 7F). Monocytes and moCs present in the per-lavg and omentum (defined as shown in Figures S4B and S4C) also increased in WT mice, and were almost undetectable in *Ccr2*$^{-/-}$ mice (Figure 7F).

The low number and location of LPMs in d4 aggregates supported that resMϕ-aggregates were disrupted, and that macrophage aggregates detectable at this stage represent the remnants of the original resMϕ-aggregates. In this regard, harvesting resMϕ-aggregates present at 4 h required a strong per-lavg, and could not be achieved by a conventional (gentle) lavage (Figures 7G–7I). In contrast, resMϕ-aggregates present at d2 were equally retrievable by a gentle or strong per-lavg (Figure 7I), revealing that they were loosely bound to the mesothelium and have started to disorganize, supporting that at d4 resMϕ-aggregates were already disrupted. ResMϕ-aggregates were not retrievable at d4, confirming that macrophage aggregates present at d4 were the remnants of disrupted resMϕ-aggregates. Since resMϕ-aggregate formation depended on a

(I1 and I2) F4/80/DAPI (I1) and GSDMD (I2) staining.
(J) Quantification of LPMs displaying a GSDMD^{bright} staining correlating with pore formation as shown in (I1) and (I2), performed by counting 60 LPMs/field in 10 CF images.
(K) CF of a non-infected per-lavg cytospin preparation.
(K1 and K2) F4/80/DAPI (K1) and GSDMD (K2) staining.
(L) WB analysis of LPM expression of GSDMD and NT-p30 GSDMD.
(M) WB analysis of LPM expression of pro-caspase-1 and cl-casp1.
(N) WB analysis of LMP expression of pro-IL-1β, and IL-1β p17.
(O) Absolute number/mouse of viable and dead LPMs in per-lavg of WT and caspase 1/11$^{-/-}$ mice. Data expressed as means ± SDs of 5 mice/condition. Similar results were obtained in 2–3 independent experiments. *, $p < 0.05$; **, $p < 0.01$; ***, $p < 0.001$

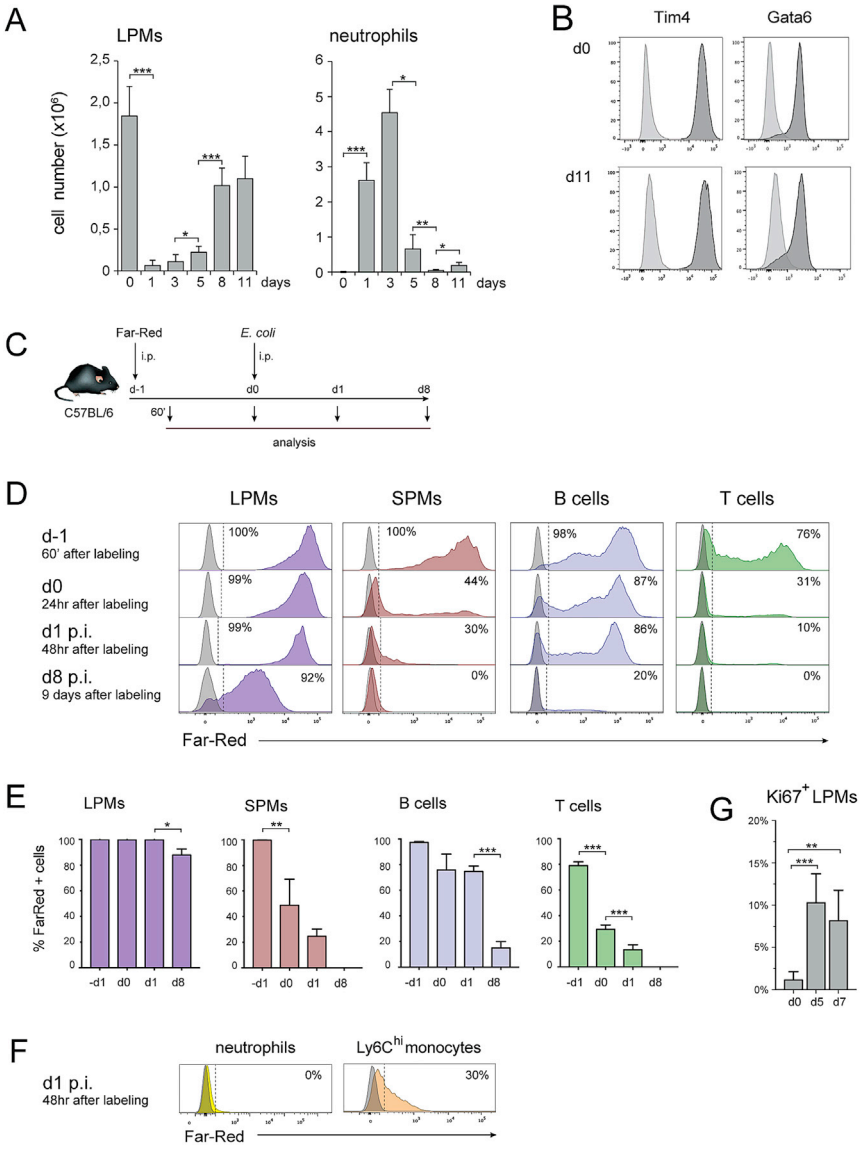

Figure 6. Kinetics of LPMs during the resolution of *E. coli* infection

(A) LPM and neutrophil absolute number in per-lavg.

(B) Tim4 and Gata6 expression by LPMs; light gray profiles: isotype control staining.

(C) Protocol of FACS analysis of peritoneal cells after Far-Red *in vivo* labeling and *E. coli* infection.

(D and E) FACS analysis (D) and quantification (E) of Far-Red labeling of LPMs, SPMs, B cells, and T cells as described in (C); the % of Far-Red$^+$ cells is indicated.

(F) Far-Red labeling of neutrophils and monocytes at d1.

(G) Ki67 expression by LPMs in per-lavg.

Gray profiles in (D) and (F): background staining. Data expressed as means ± SDs of 5 mice/condition. Similar results were obtained in at least 3 independent experiments. *, $p < 0.05$; **, $p < 0.01$; ***, $p < 0.001$

fibrin network, the disruption of resMϕ-aggregates would require the disintegration of this network through fibrin degradation, a process called fibrinolysis. Fibrinolysis is initiated by the binding of plasminogen to its receptors at the cell surface, where plasminogen activators catalyze plasminogen conversion into plasmin, the serine protease that cleaves fibrin polymers leading to fibrin degradation (Chapin and Hajjar, 2015). Analysis of 4 h and d1 resMϕ-aggregates revealed that whereas the former were compact structures possessing a developed fibrin network, the latter were loose aggregates with a partially disintegrated fibrin network and harbor a high proportion of macrophages containing phagocytosed dead cells and fibrin (Figures 7J, S5A, and S5B). Accordingly, in d1 resMϕ-aggregates, degraded fibrin was detectable in the intercellular spaces and in endocytic vesicles inside macrophages (Figures S5C–S5C2, S5D, and S5D1). Interestingly, d1 resMϕ-aggregates of WT contained moCs, not detectable at 4 h, indicating that moC actively migrated into resMϕ-aggregates (Figure 7K). As expected, very few moCs were detectable in d1 resMϕ-aggregates in *Ccr2*$^{-/-}$ mice (Figure 7L). The presence of fibrin in the cytoplasm of LPMs and moCs in d1 resMϕ-aggregates (Figures 7M, 7M1, 7N, and 7N1) supports that both cell types contributed to fibrin uptake and degradation, and that at d1, fibrinolysis was initiated. Accordingly, both LPMs and moCs expressed mRNA for Plg-RKT (Figure 7O), a membrane receptor involved in plasminogen activation at the cell surface (Andronicos et al., 2010). Whereas in d4 resMϕ-aggregate remnants, the fibrin network was profoundly degraded (Figures 7P–7P2), in *Ccr2*$^{-/-}$ mice, a well-developed fibrin network was present at d4 (Figures 7Q–7Q2 and 7R). This was not the result of differential infection kinetics, since WT and *Ccr2*$^{-/-}$ mice had comparable bacterial loads (Figure 7S). Furthermore, in *Ccr2*$^{-/-}$ mice, the number of fibrin-containing cells in d1 and d2 resMϕ-aggregates was lower than in WT mice (Figure 7T) and the size of d2 resMϕ-aggregates was larger (Figures 7U and 7V). Since the proinflammatory effect of fibrin must be blocked during the resolution of infection to prevent overt inflammation, we hypothesized that the defective fibrinolysis displayed by *Ccr2*$^{-/-}$ mice would lead to a deficient resolution of inflammation. The number of neutrophils in the per-lavg and per-wall of WT mice peaked at d2 and returned to basal levels by d4. In contrast, *Ccr2*$^{-/-}$ mice maintained high levels of peritoneal neutrophilia up to d4 (Figure S6A). The analysis of cytokine and chemokines present in the peritoneal cavity of WT mice confirmed that many inflammatory cytokines, growth and survival factors, and chemokines were detected at 4 h but disappeared by d2, supporting that peritoneal inflammation was dampened (Figures S6B–S6D). In contrast, *Ccr2*$^{-/-}$ mice maintained high levels of several inflammatory cytokines and chemokines by d2 p.i. (Figures S6C and S6E), revealing that

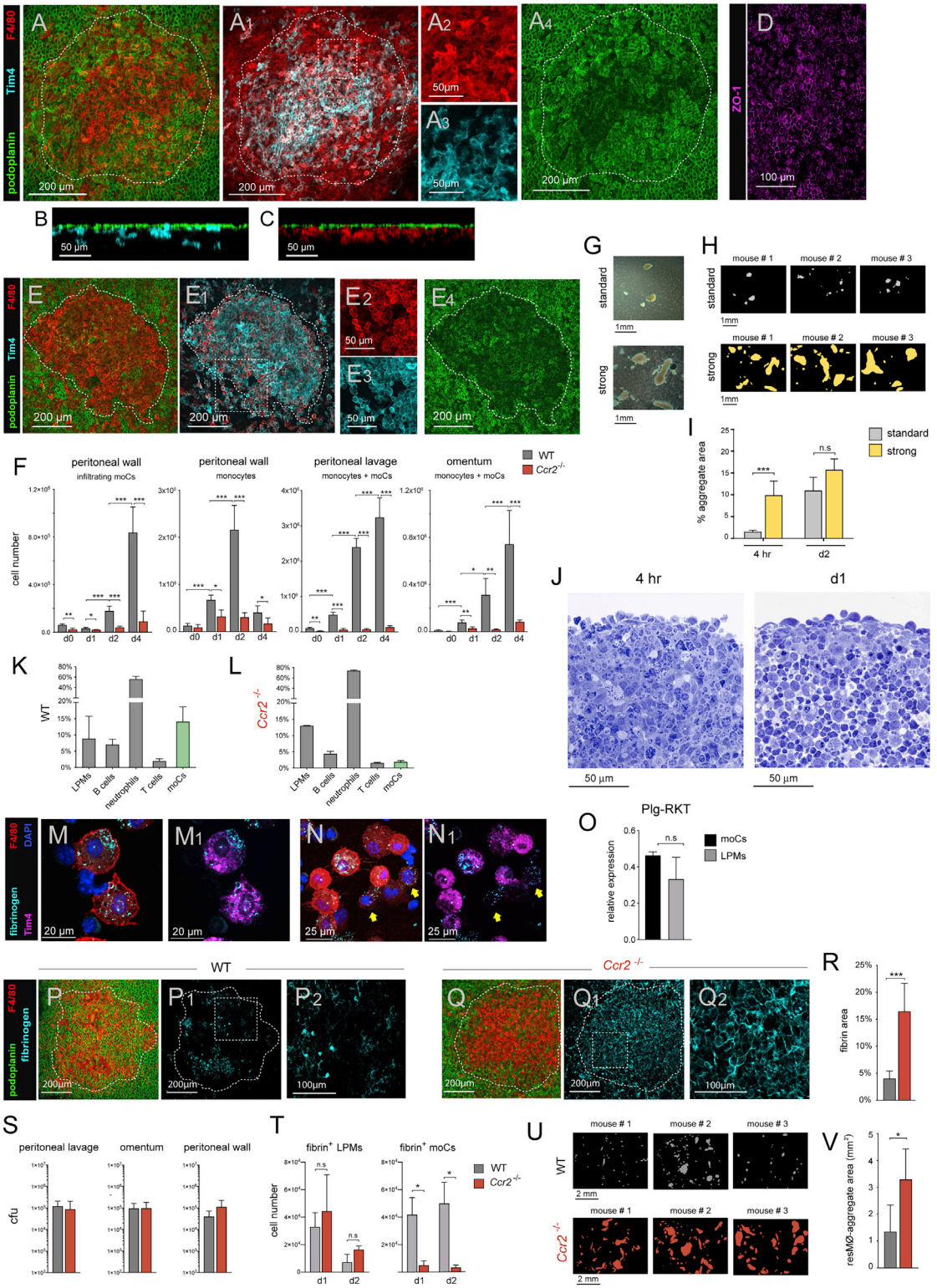

Figure 7. moCs are essential for fibrinolysis-dependent resMϕ-aggregate disruption and control of inflammation

(A and A1) WMI + CF of the remnant of a resMϕ-aggregate of a B6 mouse showing F4/80^{int} Tim4^{-} macrophages and a reduced number of F4/80^{bright} Tim4^{+} LPMs.

(A2 and A3) Enlargement of (A1).

(A4) Podoplanin staining of the area shown in (A).

(B and C) Orthogonal images of the macrophage aggregate shown in (A); podoplanin/Tim4 staining (B) and podoplanin/F4/80 staining (C).

(legend continued on next page)

peritoneal inflammation was inefficiently controlled. These data support that during the resolution of infection, moCs fulfilled an essential function in fibrin network degradation and control of inflammation. An integrated model of the formation and evolution of resMϕ-aggregates is represented in Figure S7.

DISCUSSION

Although LPMs have been classically linked to peritoneal homeostasis through the elimination of apoptotic and senescent cells, regulation of peritoneal fluid surfactant, transforming growth factor β (TGF-β)-dependent support of intestinal lamina propria B1 cell immunoglobulin A (IgA) class switch, and immunosurveillance (Bain and Jenkins, 2018), here, we show that LPMs have an essential role in defense against i.p. infection by *E. coli*. LPMs carry out a direct microbicidal function and coordinate several additional processes that lead to effective control of the infection, through the formation of mesothelium-bound, dynamic immune scaffolds, or resMϕ-aggregates. These structures are dependent on a TF-mediated fibrin network and are formed by sequentially recruited resident (LPMs and B1 cells) and inflammatory peritoneal cells (neutrophils and moCs).

Our data revealed that LPMs from *LysM-Gata6*$^{-/-}$ mice displayed a 50% reduction in number compared to WT mice, but had a comparable peritoneal bacterial load and ability to internalize *E. coli*. *Gata6*$^{-/-}$ LPMs have a lower survival and an alternative activation-biased metabolic profile (Gautier et al., 2014; Rosas et al., 2014), but data on their role against microbial infection are controversial. A higher peritoneal load was reported after i.p. *E. coli* infection, although a 2-fold higher infection dose was used in this report (Zhang et al., 2019). In contrast, no differences in peritoneal bacterial load were found between *Gata6*$^{-/-}$ and WT mice, after i.v. *Staphylococcus aureus* infection (Jorch et al., 2019). Although this result was claimed to reflect the higher neutrophil recruitment observed in *Gata6*$^{-/-}$ mice, we found no differences in peritoneal bacterial load between neutrophil-depleted *LysM-Gata6*$^{-/-}$ and WT mice. Additional experiments are thus needed to ascertain how *Gata6*$^{-/-}$ mice efficiently controlled *E. coli* infection.

Analyses by WMI + CF, electron microscopy, flow cytometry, assessment of bacterial load within resMϕ-aggregates, and experiments in which fibrin formation was prevented, demonstrate that resMϕ-aggregates are crucial against *E. coli* infection, by achieving effective containment and elimination of bacteria, thereby preventing pathogen spread. ResMϕ-aggregates are dynamic and transient structures that are disaggregated by a fibrinolysis-dependent process during the resolution of infection. Since in homeostasis, peritoneal immune cells are suspended in a fluidic environment, resMϕ-aggregates provide physical support for peritoneal immune cells and generate a cellular microenvironment that allows them to fulfill their specific defense mechanisms and to establish functional interactions. Pioneer electron microscopy studies on the MDR described that peritoneal macrophages adhere to the mesothelium of the diaphragm in response to bacterial toxin (Leak, 1985). In addition, clots of macrophages, free in the peritoneal cavity, are formed in response to i.p. administration of zymosan or *E. coli* (Zhang et al., 2019). Zymosan-induced clots are composed essentially of macrophages and neutrophils; their formation was proposed to depend on coagulation factor V produced by LPMs, and was prevented by combining the blockade of coagulation and integrin-mediated adhesion. Clots formed in response to *E. coli* efficiently contribute to bacterial clearance, but neither their cellular structure, composition, and dynamics nor their evolution during infection were described. The fact that zymosan causes the formation of macrophage-neutrophil clots not attached to the mesothelium may reflect that the 1-mg/mouse high dose of zymosan used in this study leads to a massive death of resident peritoneal macrophages; this would preclude their adhesion to the

(D) ZO1 staining of a resMϕ-aggregate remnant at d4.
(E and E1) Per-wall WMI + CF of a *Ccr2*$^{-/-}$ mouse at d4.
(E2 and E3) Enlargement of (E1).
(E4) Podoplanin staining of the area shown in (E).
(F) Absolute number/mouse of the indicated subsets in per-wall, per-lavg, and omentum in WT and *Ccr2*$^{-/-}$ mice.
(G) Phase contrast micrographs of resMϕ-aggregates harvested by standard or strong per-lavg at 4 h.
(H) Phase contrast micrographs processed to quantify the resMϕ-aggregate area/micrograph after standard or strong per-lavg at 4 h.
(I) ResMϕ-aggregate area/micrograph after standard or strong per-lavg at 4 h and d2, performed on micrographs processed as shown in (H); data expressed as mean percentage of resMϕ-aggregates area/micrograph ± SDs of 4 micrographs/condition.
(J) Semi-thin sections of resMϕ-aggregates at 4 h and d1.
(K and L) Relative proportion of the indicated cell types present in resMϕ-aggregates of WT and *Ccr2*$^{-/-}$ mice at d1; FACS analysis.
(M and M1) High magnification CF image of a disaggregated resMϕ-aggregate cytospin preparation at d1, showing fibrin in LPMs.
(N and N1) CF of a resMϕ-aggregate cytospin preparation at d1, showing fibrin in F4/80^{bright} Tim4^{+} LPMs and F4/80^{int} Tim4^{-} moCs (yellow arrows).
(O) Plg-RKT mRNA expression by FACS-sorted LPMs and d1 moCs analyzed by real-time PCR normalized to β-actin.
(P and P1) WMI + CF of a resMϕ-aggregate remnant of a WT mouse at d4.
(P2) Enlargement of (P1).
(Q and Q1) WMI + CF of a resMϕ-aggregate of a Ccr2$^{-/-}$ mouse at d4.
(Q2) Enlargement of (Q1).
(R) Area occupied by fibrin in resMϕ-aggregates in WT and *Ccr2*$^{-/-}$ mice at d4; mean percentage of fibrin staining/micrograph ± SDs of 5 micrographs/condition.
(S) Bacterial load in the per-lavg, omentum, and per-wall of WT and Ccr2$^{-/-}$ mice at d1.
(T) Quantification of LPMs and moCs containing fibrin in resMϕ-aggregates at d1 and d2 analyzed by FACS in disaggregated resMϕ-aggregates.
(U) Phase contrast micrographs processed to quantify the resMϕ-aggregate area/micrograph after strong per-lavg in WT and *Ccr2*$^{-/-}$ mice, at d4.
(V) ResMϕ-aggregate area/mouse after strong per-lavg in WT and Ccr2$^{-/-}$ mice, at d4, performed in micrographs processed as shown in (U); mean area occupied by resMϕ-aggregates in each micrograph ± SD of 4 micrographs/condition. Data expressed as means ± SDs of 5 mice/condition. Similar results were obtained in at least 3 independent experiments. *, $p < 0.05$; **, $p < 0.01$; ***, $p < 0.001$
See also Figures S4–S6.

mesothelium, since high-dose zymosan causes the complete ablation of LPMs (Louwe et al., 2021). Interestingly, high-dose zymosan (0.5 mg/mouse) triggers the formation of milky spot-associated neutrophil aggregates (Jackson-Jones et al., 2020), claimed to provide a relay for the clearance of peritoneal contaminants to peritoneal macrophages, described, as mentioned above, to be rapidly sequestered in clots after high-dose zymosan (Zhang et al., 2019). This conclusion contrasts with our results revealing that *E. coli* infection promoted the formation of milky spot-associated aggregates essentially formed by LPMs and a lower proportion of neutrophils, and provide an alternative explanation to the relay hypothesis, by which peritoneal macrophages were absent from neutrophil aggregates due to their low survival after high-dose zymosan treatment. It is worth noting that resident peritoneal macrophages function as extravascular platelets by forming thrombus-like structures in response to laser-induced mesothelial injury, leading to a rapid repair of focal lesions (Zindel et al., 2021). The formation of these macrophage aggregates after peritoneal injury is not prevented by thrombin inhibitors or antibodies against canonical adhesion molecules and is dependent on primordial scavenger receptor cysteine-rich (SRCR) domains, revealing that resident peritoneal macrophages use diverse molecular mechanisms to perform different functions.

Research over the last decades has established that TF plays an essential role in sepsis-associated disseminated intravascular coagulation (DIC), and that TF from monocytes has a prominent role in DIC in mouse models of sepsis (Gando et al., 2016; Grover and Mackman, 2018). We found that TF was expressed by mesothelial cells before and after infection, but was not detectable in LPMs. Pleural and peritoneal mesothelial cells express TF under pathological conditions, including fibrosis, cancer, dialysis, and surgery (Mutsaers et al., 2016); however, the fact that it is constitutively expressed by the peritoneal mesothelium is a key finding of our study. TF is expressed by bone marrow-derived macrophages after *in vitro* inflammasome activation (Wu et al., 2019) or LPS stimulation (Rothmeier et al., 2015) and by peritoneal macrophages at 6 h of lipopolysaccharide (LPS) treatment (Ahamed et al., 2007). Our data revealed that LPMs did not express TF before or along the first 4 h after infection and suggest that mesothelial cells are the primary source of TF-triggering coagulation and fibrin polymerization in resMϕ-aggregates. Along this line, TF from nonhematopoietic cells contributes to the activation of coagulation in mouse models of endotoxemia (Cheng et al., 2017; Pawlinski et al., 2010).

Fibrin has a strong proinflammatory potential by regulating, direct and indirectly, multiple leukocyte effector functions, such as migration, phagocytosis, and cytokine and chemokine production (Luyendyk et al., 2019). Fibrin-Mac-1 interactions are crucial for bacterial clearance (Flick et al., 2004) and enhance microglia phagocytic capacity (Adams et al., 2007), supporting that the interaction of Mac-1 on LPMs with fibrin promotes efficient bacterial uptake and killing by LPMs within resMϕ-aggregates. TF-dependent fibrin deposition has a protective role in microbial infections (Flick et al., 2004; Johnson et al., 2003; Luo et al., 2011). In addition, fibrin, acting as a bridging molecule binding to Mac-1 and ICAM-1 may favor leukocyte-leukocyte and leukocyte-mesothelium interactions.

During the resolution of infection, after resMϕ-aggregates had completed their bacteria containment and elimination function, dead cells must be removed, the proinflammatory effect of fibrin neutralized, and resMϕ-aggregates disrupted, allowing the dampening of inflammation, incorporation of viable immune cells to the peritoneal cavity, and mesothelial repair. Disruption of resMϕ-aggregates required the disintegration of the fibrin network, and correspondingly, a high proportion of LPMs and moCs present in resMϕ-aggregates contained degraded fibrin in endolysosomal vesicles, supporting their contribution to fibrinolysis through fibrin endocytosis and lysosomal degradation. Interestingly, a novel extravascular fibrinolysis mechanism by which fibrin partially degraded extracellularly is endocytosed and subjected to lysosomal complete degradation was described after subcutaneous implantation of fibrin gels (Motley et al., 2016). This process was proposed to rely mainly on $CCR2^{+}$ macrophages and to involve receptor-mediated plasminogen binding and activation at the cell surface. Interestingly, the integral membrane receptor Plg-RKT, a major regulator of cell surface plasminogen activation (Andronicos et al., 2010), was expressed by LPMs and moCs, supporting their role in extracellular fibrinolysis involving endocytosis and lysosomal degradation of partially degraded fibrin.

The deficient fibrinolysis occurring in $Ccr2^{-/-}$ mice was paralleled by high levels of peritoneal neutrophilia and a defective dampening of inflammation, supporting the importance of moCs in fibrin degradation and control of inflammation. Importantly, moC recruitment to resMϕ-aggregates was dependent on LPMs that also controlled leukocyte recruitment to milky spots, a process that may be required for the induction of the additional defense mechanisms directed at the complete resolution of the infection.

The present study reveals that LPMs are crucial for immunity against i.p. *E. coli* infection by fulfilling and coordinating several processes resulting in an effective control of infection. LPMs efficiently achieve bacterial clearance, promote the formation of resMϕ-aggregates, induce the recruitment of monocytes to these structures, participate in dead cell removal and fibrinolysis-mediated resident macrophage aggregate disruption, and control omental milky spot expansion. Our data emphasize an essential immune-mesothelium cooperation and hint that defense against i.p. *E. coli* infection relies on complex coagulation-inflammation-immunity interactions requiring the formation of resMϕ-aggregates. The formation of similar structures may also occur during infection in other body cavities, such as the pleural cavity or the brain ventricular system, harboring macrophages in a fluidic environment, which may need to attach to the epithelium lining these cavities to fulfill their immune defense functions.

Limitations of the study

The present study reveals that peritoneal immune cells, free in a fluidic environment in homeostatic conditions, require organization in complex and dynamic resMϕ-aggregates to interact and fulfill their specific immune functions, during defense against bacterial infection. Whether similar structures are formed in patients during the early phases of abdominal sepsis still must be proven, but will be particularly challenging due to technical limitations. Additional experimental work will be

needed to demonstrate whether resMϕ-aggregate formation is restricted to peritoneal bacterial infections or reflects a general mechanism by which immune cells located in body cavities fight against pathogens. In this regard, preliminary experiments performed by our group confirmed that bacterial infection induced the formation of resMϕ-aggregate-like structures in the pleural cavity. Our data strongly support that thrombin-driven fibrin polymerization is required for resMϕ-aggregate formation, but how TF is activated as a result of the interaction between LPMs and mesothelial cells has to be investigated.. Finally, the potential role in defense against peritoneal infection of B1 cells, a major component of resMϕ-aggregates, remains unexplored.

STAR★METHODS

Detailed methods are provided in the online version of this paper and include the following:

- KEY RESOURCES TABLE
- RESOURCE AVAILABILITY
  - Lead contact
  - Materials availability
  - Data and code availability
- EXPERIMENTAL MODEL AND SUBJECT DETAILS
  - Mice
- METHOD DETAILS
  - *E. coli* infection
  - CSI
  - Bacterial burden determination
  - Per-lavg
  - Cell suspensions
  - LPM purification
  - Mesothelial cell isolation
  - Cytospin preparations
  - Analysis of serum enzymes
  - LPM depletion
  - Neutrophil depletion
  - *In vivo* treatment with heparin and hirudin
  - *In vitro* LPM adherence assay
  - Transfer of peritoneal cells
  - *In vivo* cell fluorescent labeling
  - Cytokine and chemokine profiling
  - Flow cytometry
  - Whole mount immunofluorescence (WMI)
  - Immunofluorescent staining of cytospin slides
  - Electron microscopy
  - Western blot
  - RNA extraction and real-time PCR
- QUANTIFICATION AND STATISTICAL ANALYSIS

SUPPLEMENTAL INFORMATION

Supplemental information can be found online at https://doi.org/10.1016/j.immuni.2021.10.007.

ACKNOWLEDGMENTS

We thank E. Veiga and P. Pelegrín for experimental advice and the Advanced Light Microscopy and the Electron Microscopy facilities of the CNB for technical advice and sample processing. This work was supported by grants SAF2015-69905, PGC2018-101899-B-100, and S2017/BMD3731 to C.A. and grant PID2019-104399RB-100 to G.S. The CNIC is supported by the Instituto de Salud Carlos III, Ministerio de Ciencia e Innovación, and the Pro CNIC Foundation.

AUTHOR CONTRIBUTIONS

C.A. designed the research, analyzed the data, and wrote the manuscript. M.L.-B. designed the research, performed the experiments, and analyzed the data. L.H.V. and A.V.-P. performed most of the experiments and analyzed the data. C.G. performed the western blot and electron microscopy experiments. A.G.-G., L.F.-L., M.F., N.M.-P., and J.A. assisted in the experiments. G.S. and A.M. analyzed the serum enzymes.

DECLARATION OF INTERESTS

The authors declare no competing interests.

Received: April 20, 2021
Revised: June 13, 2021
Accepted: October 11, 2021
Published: October 29, 2021

REFERENCES

Adams, R.A., Bauer, J., Flick, M.J., Sikorski, S.L., Nuriel, T., Lassmann, H., Degen, J.L., and Akassoglou, K. (2007). The fibrin-derived γ377-395 peptide inhibits microglia activation and suppresses relapsing paralysis in central nervous system autoimmune disease. J. Exp. Med. *204*, 571–582.

Ahamed, J., Niessen, F., Kurokawa, T., Lee, Y.K., Bhattacharjee, G., Morrissey, J.H., and Ruf, W. (2007). Regulation of macrophage procoagulant responses by the tissue factor cytoplasmic domain in endotoxemia. Blood *109*, 5251–5259.

Andronicos, N.M., Chen, E.I., Baik, N., Bai, H., Parmer, C.M., Kiosses, W.B., Kamps, M.P., Yates, J.R., 3rd, Parmer, R.J., and Miles, L.A. (2010). Proteomics-based discovery of a novel, structurally unique, and developmentally regulated plasminogen receptor, Plg-RKT, a major regulator of cell surface plasminogen activation. Blood *115*, 1319–1330.

Angus, D.C., and van der Poll, T. (2013). Severe sepsis and septic shock. N. Engl. J. Med. *369*, 840–851.

Bain, C.C., and Jenkins, S.J. (2018). The biology of serous cavity macrophages. Cell. Immunol. *330*, 126–135.

Bain, C.C., Hawley, C.A., Garner, H., Scott, C.L., Schridde, A., Steers, N.J., Mack, M., Joshi, A., Guilliams, M., Mowat, A.M.I., et al. (2016). Long-lived self-renewing bone marrow-derived macrophages displace embryo-derived cells to inhabit adult serous cavities. Nat. Commun. *7*, ncomms11852.

Barth, M.W., Hendrzak, J.A., Melnicoff, M.J., and Morahan, P.S. (1995). Review of the macrophage disappearance reaction. J. Leukoc. Biol. *57*, 361–367.

Bénézech, C., Luu, N.T., Walker, J.A., Kruglov, A.A., Loo, Y., Nakamura, K., Zhang, Y., Nayar, S., Jones, L.H., Flores-Langarica, A., et al. (2015). Inflammation-induced formation of fat-associated lymphoid clusters. Nat. Immunol. *16*, 819–828.

Buscher, K., Wang, H., Zhang, X., Striewski, P., Wirth, B., Saggu, G., Lütke-Enking, S., Mayadas, T.N., Ley, K., Sorokin, L., and Song, J. (2016). Protection from septic peritonitis by rapid neutrophil recruitment through omental high endothelial venules. Nat. Commun. *7*, 10828.

Chapin, J.C., and Hajjar, K.A. (2015). Fibrinolysis and the control of blood coagulation. Blood Rev. *29*, 17–24.

Cheng, K.T., Xiong, S., Ye, Z., Hong, Z., Di, A., Tsang, K.M., Gao, X., An, S., Mittal, M., Vogel, S.M., et al. (2017). Caspase-11-mediated endothelial pyroptosis underlies endotoxemia-induced lung injury. J. Clin. Invest. *127*, 4124–4135.

Engel, D.R., Maurer, J., Tittel, A.P., Weisheit, C., Cavlar, T., Schumak, B., Limmer, A., van Rooijen, N., Trautwein, C., Tacke, F., and Kurts, C. (2008).

CCR2 mediates homeostatic and inflammatory release of Gr1(high) monocytes from the bone marrow, but is dispensable for bladder infiltration in bacterial urinary tract infection. J. Immunol. *181*, 5579–5586.

Flick, M.J., Du, X., Witte, D.P., Jirousková, M., Soloviev, D.A., Busuttil, S.J., Plow, E.F., and Degen, J.L. (2004). Leukocyte engagement of fibrin(ogen) via the integrin receptor alphaMbeta2/Mac-1 is critical for host inflammatory response in vivo. J. Clin. Invest. *113*, 1596–1606.

Gando, S., Levi, M., and Toh, C.H. (2016). Disseminated intravascular coagulation. Nat. Rev. Dis. Primers *2*, 16037.

Gautier, E.L., Ivanov, S., Williams, J.W., Huang, S.C.-C., Marcelin, G., Fairfax, K., Wang, P.L., Francis, J.S., Leone, P., Wilson, D.B., et al. (2014). Gata6 regulates aspartoacylase expression in resident peritoneal macrophages and controls their survival. J. Exp. Med. *211*, 1525–1531.

Grover, S.P., and Mackman, N. (2018). Tissue Factor: An Essential Mediator of Hemostasis and Trigger of Thrombosis. Arterioscler. Thromb. Vasc. Biol. *38*, 709–725.

Jackson-Jones, L.H., Smith, P., Portman, J.R., Magalhaes, M.S., Mylonas, K.J., Vermeren, M.M., Nixon, M., Henderson, B.E.P., Dobie, R., Vermeren, S., et al. (2020). Stromal Cells Covering Omental Fat-Associated Lymphoid Clusters Trigger Formation of Neutrophil Aggregates to Capture Peritoneal Contaminants. Immunity *52*, 700–715.e6.

Johnson, L.L., Berggren, K.N., Szaba, F.M., Chen, W., and Smiley, S.T. (2003). Fibrin-mediated protection against infection-stimulated immunopathology. J. Exp. Med. *197*, 801–806.

Jorch, S.K., Surewaard, B.G.J., Hossain, M., Peiseler, M., Deppermann, C., Deng, J., Bogoslowski, A., van der Wal, F., Omri, A., Hickey, M.J., and Kubes, P. (2019). Peritoneal GATA6+ macrophages function as a portal for Staphylococcus aureus dissemination. J. Clin. Invest. *129*, 4643–4656.

Jorgensen, I., Rayamajhi, M., and Miao, E.A. (2017). Programmed cell death as a defence against infection. Nat. Rev. Immunol. *17*, 151–164.

Kayagaki, N., Stowe, I.B., Lee, B.L., O'Rourke, K., Anderson, K., Warming, Sø., Cuellar, T., Haley, B., Roose-Girma, M., Phung, Q.T., et al. (2015). Caspase-11 cleaves gasdermin D for non-canonical inflammasome signalling. Nature *526*, 666–671.

Khan, W.N., Alt, F.W., Gerstein, R.M., Malynn, B.A., Larsson, I., Rathbun, G., Davidson, L., Müller, S., Kantor, A.B., Herzenberg, L.A., et al. (1995). Defective B cell development and function in Btk-deficient mice. Immunity *3*, 283–299.

Kuida, K., Lippke, J.A., Ku, G., Harding, M.W., Livingston, D.J., Su, M.S.S., and Flavell, R. (1995). Altered cytokine export and apoptosis in mice deficient in interleukin-1β converting enzyme. Science *267*, 2000–2003.

Leak, L.V. (1985). Interaction of the peritoneal cavity to intraperitoneal stimulation: a peritoneal model system to monitor cellular and extracellular events in the formation of granulation tissue. Am. J. Anat. *173*, 171–183.

Lever, R., and Page, C.P. (2002). Novel drug development opportunities for heparin. Nat. Rev. Drug Discov. *1*, 140–148.

Lewis, A.J., Seymour, C.W., and Rosengart, M.R. (2016). Current Murine Models of Sepsis. Surg. Infect. (Larchmt.) *17*, 385–393.

Louwe, P.A., Badiola Gomez, L., Webster, H., Perona-Wright, G., Bain, C.C., Forbes, S.J., and Jenkins, S.J. (2021). Recruited macrophages that colonize the post-inflammatory peritoneal niche convert into functionally divergent resident cells. Nat. Commun. *12*, 1770.

Luo, D., Szaba, F.M., Kummer, L.W., Plow, E.F., Mackman, N., Gailani, D., and Smiley, S.T. (2011). Protective roles for fibrin, tissue factor, plasminogen activator inhibitor-1, and thrombin activatable fibrinolysis inhibitor, but not factor XI, during defense against the gram-negative bacterium Yersinia enterocolitica. J. Immunol. *187*, 1866–1876.

Luyendyk, J.P., Schoenecker, J.G., and Flick, M.J. (2019). The multifaceted role of fibrinogen in tissue injury and inflammation. Blood *133*, 511–520.

Meza-Perez, S., and Randall, T.D. (2017). Immunological Functions of the Omentum. Trends Immunol. *38*, 526–536.

Motley, M.P., Madsen, D.H., Jürgensen, H.J., Spencer, D.E., Szabo, R., Holmbeck, K., Flick, M.J., Lawrence, D.A., Castellino, F.J., Weigert, R., and Bugge, T.H. (2016). A CCR2 macrophage endocytic pathway mediates extravascular fibrin clearance in vivo. Blood *127*, 1085–1096.

Mutsaers, S.E., Birnie, K., Lansley, S., Herrick, S.E., Lim, C.B., and Prêle, C.M. (2015). Mesothelial cells in tissue repair and fibrosis. Front. Pharmacol. *6*, 113.

Mutsaers, S.E., Prêle, C.M.A., Pengelly, S., and Herrick, S.E. (2016). Mesothelial cells and peritoneal homeostasis. Fertil. Steril. *106*, 1018–1024.

Okabe, Y., and Medzhitov, R. (2014). Tissue-specific signals control reversible program of localization and functional polarization of macrophages. Cell *157*, 832–844.

Opal, S.M., Garber, G.E., LaRosa, S.P., Maki, D.G., Freebairn, R.C., Kinasewitz, G.T., Dhainaut, J.F., Yan, S.B., Williams, M.D., Graham, D.E., et al. (2003). Systemic host responses in severe sepsis analyzed by causative microorganism and treatment effects of drotrecogin alfa (activated). Clin. Infect. Dis. *37*, 50–58.

Pawlinski, R., Wang, J.G., Owens, A.P., 3rd, Williams, J., Antoniak, S., Tencati, M., Luther, T., Rowley, J.W., Low, E.N., Weyrich, A.S., and Mackman, N. (2010). Hematopoietic and nonhematopoietic cell tissue factor activates the coagulation cascade in endotoxemic mice. Blood *116*, 806–814.

Rathkey, J.K., Benson, B.L., Chirieleison, S.M., Yang, J., Xiao, T.S., Dubyak, G.R., Huang, A.Y., and Abbott, D.W. (2017). Live-cell visualization of gasdermin D-driven pyroptotic cell death. J. Biol. Chem. *292*, 14649–14658.

Rosas, M., Davies, L.C., Giles, P.J., Liao, C.-T., Kharfan, B., Stone, T.C., O'Donnell, V.B., Fraser, D.J., Jones, S.A., and Taylor, P.R. (2014). The transcription factor Gata6 links tissue macrophage phenotype and proliferative renewal. Science *344*, 645–648.

Rothmeier, A.S., Marchese, P., Petrich, B.G., Furlan-Freguia, C., Ginsberg, M.H., Ruggeri, Z.M., and Ruf, W. (2015). Caspase-1-mediated pathway promotes generation of thromboinflammatory microparticles. J. Clin. Invest. *125*, 1471–1484.

Shi, C., and Pamer, E.G. (2011). Monocyte recruitment during infection and inflammation. Nat. Rev. Immunol. *11*, 762–774.

Vincent, J.L., Rello, J., Marshall, J., Silva, E., Anzueto, A., Martin, C.D., Moreno, R., Lipman, J., Gomersall, C., Sakr, Y., and Reinhart, K.; EPIC II Group of Investigators (2009). International study of the prevalence and outcomes of infection in intensive care units. JAMA *302*, 2323–2329.

Wu, C., Lu, W., Zhang, Y., Zhang, G., Shi, X., Hisada, Y., Grover, S.P., Zhang, X., Li, L., Xiang, B., et al. (2019). Inflammasome Activation Triggers Blood Clotting and Host Death through Pyroptosis. Immunity *50*, 1401–1411.e4.

Zeng, M.Y., Cisalpino, D., Varadarajan, S., Hellman, J., Warren, H.S., Cascalho, M., Inohara, M., and Núñez, G. (2016). Gut Microbiota-Induced Immunoglobulin G Controls Systemic Infection by Symbiotic Bacteria and Pathogens. Immunity *44*, 647–658.

Zhang, N., Czepielewski, R.S., Jarjour, N.N., Erlich, E.C., Esaulova, E., Saunders, B.T., Grover, S.P., Cleuren, A.C., Broze, G.J., Edelson, B.T., et al. (2019). Expression of factor V by resident macrophages boosts host defense in the peritoneal cavity. J. Exp. Med. *216*, 1291–1300.

Zindel, J., Peiseler, M., Hossain, M., Deppermann, C., Lee, W.Y., Haenni, B., Zuber, B., Deniset, J.F., Surewaard, B.G.J., Candinas, D., and Kubes, P. (2021). Primordial GATA6 macrophages function as extravascular platelets in sterile injury. Science *371*, eabe0595.

STAR★METHODS

KEY RESOURCES TABLE

REAGENT or RESOURCE	SOURCE	IDENTIFIER
Antibodies		
CD11b, PE-Cy7-conjugate, clone M1/70	eBioscience	Cat # 25-0112-81; RRID:AB_469587
CD11c, APC-Cy7-conjugate, clone HL3	BD Biosciences	Cat # 561241; RRID:AB_10611727
CD19, PE-conjugate, clone 1D3	BD Biosciences	Cat # 553786; RRID:AB_395050
CD45, Pacific Blue-conjugate, clone 30-F11	BioLegend	Cat # 103126; RRID:AB_493535
CD90.2, PE-conjugate, clone 53-2.1	BD Biosciences	Cat # 553006; RRID:AB_394545
F4/80, FITC-conjugate, clone BM8	eBioscience	Cat # 11-4801-82; RRID:AB_2637191
Gata-6, PE-conjugate, clone D61E4	Cell Signaling	Cat # 26452S; RRID:AB_2798924
I-A/I-E, APC-conjugate, clone M5/114.15.2	eBioscience	Cat # 17-5321-81; RRID:AB_469454
-A/I-E, FITC-conjugate, clone 2G9	BD Biosciences	Cat # 553623; RRID:AB_394958
ICAM-1, FITC-conjugate, clone 3E2	BD Biosciences	Cat # 553252; RRID:AB_394734
Ki67, Alexa Fluor 647-conjugate, clone B56	BD Biosciences	Cat # 558615; RRID:AB_647130
Ly6G, PE-conjugate, clone 1A8	BD Biosciences	Cat # 551461; RRID:AB_394208
Streptavidin, APC/Cy7-conjugate	BioLegend	Cat # 405208
Streptavidin, PerCP-conjugate	BD Biosciences	Cat # 554064; RRID:AB_2336918
TF, goat polyclonal	R&D	Cat # AF3178; RRID:AB_2278143
Tim4, BV421-conjugate, clone 21H12	BD Biosciences	Cat # 742773; RRID:AB_2741037
Tim4, PE-conjugate, clone F31-5G3	BioLegend	Cat # 129905; RRID:AB_1227799
CD19, Alexa Fluor 647-conjugate, clone 6D5	BioLegend	Cat # 115522; RRID:AB_389329
Cleaved caspase-3 (D175), rabbit polyclonal	Cell signaling	Cat # 9661S; RRID:AB_2341188
F4/80, Alexa Fluor 488-conjugate, clone BM8	BioLegend	Cat # 123120; RRID:AB_893479
F4/80, Alexa Fluor 594-conjugate, clone BM8	BioLegend	Cat # 123140; RRID:AB_2563241
F4/80, Alexa Fluor 647-conjugate, clone BM8	BioLegend	Cat # 123122; RRID:AB_893480
Fibrinogen, rabbit polyclonal	Agilent Dako	Cat# A008002; RRID:AB_578481
Gasdermin-D, rabbit monoclonal, clone EPR20859	Abcam	Cat # ab219800; RRID:AB_2888940
Goat anti-rabbit Ig Fluor 546- conjugate Alexa	Thermo Fisher	Cat # A11035; RRID:AB_143051
Goat-anti-rabbit Ig, Alexa Fluor 647- conjugate	Thermo Fisher	Cat # A21245; RRID:AB_2535813
Ly6G, Alexa Fluor 647-conjugate, clone 1A8	BioLegend	Cat# 127609; RRID:AB_1134162
pMLKL (Ser345) (D6E3G), rabbit monoclonal	Cell Signaling	Cat# 91689; RRID:AB_2732034
Podoplanin, Alexa Fluor 488-conjugate, clone 8.1.1	BioLegend	Cat # 127406; RRID:AB_2161930
Tim4, Alexa Fluor 647-conjugate, clone 21H12	BD Biosciences	Cat # 564177; RRID:AB_2647750
TNF-a, Alexa Fluor 647-conjugate, clone MP6-XT22	BioLegend	Cat # 506314; RRID:AB_493330
ZO-1, Alexa Fluor 594-conjugate, clone ZO1-1A12	Invitrogen	Cat # 339194; RRID:AB_2532188
Anti-Gr1 antibody, clone RB6-8C5	BioXCell	Cat# BE0075; RRID:AB_10312146
Anti-Ly6G antibody, clone 1A8	BioXCell	Cat# BE0075-1; RRID:AB_1107721
Bacterial strains		
Escherichia coli M6L4 strain	Dr. G. Nuñez (University of Michigan)	(Zeng et al., 2016)
Chemicals, peptides, and recombinant proteins		
Liberase TL	Roche	Cat # 05401020001
Liberase TM	Roche	Cat # 05401119001
DNase I	Roche	Cat # 10104159001
Anti-rat immunoglobulin-coated magnetic beads	Thermo Fisher	Cat #11035
Clodronate-loaded liposomes	Liposoma	N/A
Heparin (unfractionated)	Rovi	N/A

(*Continued on next page*)

Continued		
REAGENT or RESOURCE	SOURCE	IDENTIFIER
Recombinant Hirudin	Aniara Diagnostica	Cat # RE120A
DAPI	Sigma-Aldrich	Cat # 28718-90-3
Trypsin	Sigma-Aldrich	Cat # 9002-07-7
Critical commercial assays		
Proteome Profiler Mouse Cytokine Array Kit, Panel A	R&D Systems	Cat # ARY006
Proteome Profiler Mouse XL Cytokine Array Kit	R&D Systems	Cat # ARY028
FITC Annexin V Apoptosis Detection Kit with 7-AAD	BioLegend	Cat # 640922
CellTrace Far Red Cell proliferation kit	Thermo Fisher	Cat #C34571
Vybrant CFDA SE. Cell Tracer Kit	Invitrogen	Cat # V12883
eBioscience Foxp3/Transcription Factor Staining buffer Set	Thermo Fisher	Cat# 00-5523-00
BD Cytofix/cytoperm kit	BD Biosciences	Cat # 554714
Experimental models: organisms/strains		
Mouse: C57BL/6 mice	Charles River	JAX000664
Mouse: Xid mice	Dr. Y. Carrasco (CNB/CSIC)	(Khan et al., 1995)
Mouse: *LysM-Gata6* $^{-/-}$	Dr. R. Medzhitov (Yale University)	(Okabe and Medzhitov, 2014)
Mouse: *Casp1/11* $^{-/-}$	Dr. P. Pelegrín (IMIB-Arrixaca)	(Kuida et al., 1995)
Mouse: *Ccr2* $^{-/-}$	Dr. F. Tacke (Hospital Aachen)	(Engel et al., 2008)
Mouse: *Gsdmd* $^{-/-}$	Dr. I. Couillin (Orléans University)	(Kayagaki et al., 2015)
Oligonucleotides		
Plg-PRK qPCR FDW	N/A	GGCAAATGGCTATGCAGATCGC
Plg-PRK qPCR REV	N/A	AGGACCGAGAAAGGCTGGCTTC
Software and algorithms		
FlowJo X	Flowjo	https://www.flowjo.com/solutions/flowjo
Prism 8	GraphPad Software	http://www.graphpad.com/scientific-software/prism/
Fiji	ImageJ	https://imagej.net/Fiji
LAS X software	Leica	htttps://www.leica-microsystems.com/products/microscope-software
Protein Array Analyzer for ImageJ	Gilles Carpentier's Dot-Blot-Analyzer macro	http://rsb.info.nih.gov/ij/macros/toolsets/ProteinArray Analyzer.txt
Other		
BD LSR II Flow Cytometer	BD Biosciences	N/A

RESOURCE AVAILABILITY

Lead contact

Further information and requests for reagents may be directed to the lead contact Carlos Ardavín (ardavin@cnb.csic.es).

Materials availability

This study did not generate new unique reagents.

Data and code availability

Any additional information required to reanalyze the data reported in this paper is available from the lead contact upon request.

EXPERIMENTAL MODEL AND SUBJECT DETAILS

Mice

C57BL/6 mice were purchased from Charles River (L'Arbresle, France). A colony of *LysM-Gata6*$^{-/-}$ (*LysM-Cre Gata6*-floxed mice; B6 background) mice was established at the Animal Facility of the Centro Nacional de Biotecnología (CNB)/CSIC from cryopreserved sperm kindly provided by Dr. R. Medzhitov (Howard Hughes Medical Institute, Yale University School of Medicine, USA). Xid mice

(CBA background) were kindly supplied by Dr. Y. Carrasco (CNB/CSIC, Spain). *Gsdmd*$^{-/-}$ mice (B6 background) were kindly supplied by Dr. I. Couillin (University of Orléans and CNRS). *Casp1/11*$^{-/-}$ mice (B6 background) were kindly supplied by Dr. P. Pelegrín (IMIB-Arrixaca, Spain). *Ccr2*$^{-/-}$ mice (B6 background) were kindly supplied by Dr. F. Tacke (RW-TH-University Hospital Aachen, Germany). Xid, *Gsdmd*$^{-/-}$ and *Ccr2*$^{-/-}$ mice were housed at the Animal Facility of CNB/CSIC, on a 12 h /12 h light/dark cycle, with free access to food and water. Littermates of the same sex were randomly assigned to experimental groups. All the experiments were approved by the Animal Care and Use Committee of the Centro Nacional de Biotecnología-CSIC, Madrid, under the protocol 363/15.

METHOD DETAILS

E. coli infection

Escherichia coli strain M6L4, isolated from the mouse intestine, was kindly provided by Dr. G. Núñez (University of Michigan Medical School, Ann Arbor, Michigan, USA). GFP-labeled *E. coli* was obtained by transformation of M6L4 *E. coli* with the PGen 22 plasmid (kindly supplied by Dr. E. Veiga, CNB/CSIC, Madrid, Spain) to constitutively express GFP. Bacteria were grown overnight in LB plates at 37°C. Mice were infected by intraperitoneal injection of 1×10^7 *E.coli* in 0.2 mL of PBS and monitored daily for health and survival following the institutional guidance.

CSI

Feces from B6 mice were resuspended in sterile PBS at 100 mg/mL, homogenized, filtered through 40-μm cell strainer (BD PharMingen), as described (Lewis et al., 2016). 200 μL/mouse of the homogenate were injected intraperitoneally.

Bacterial burden determination

Organs were aseptically removed and homogenized in PBS using a T10 basic Ultra-Turrax homogenizer (Ika). The bacterial load of the per-wall was analyzed on a cell suspension obtained after scratching its inner face using a cell scraper that was subsequently homogenized. Bacterial burden was determined by plating 25 μL tissue homogenates or 25 μL of per-lavg in serial dilutions onto LB agar plates. Colony forming units (CFUs) were counted after growth for 24 h at 37°C.

Per-lavg

Standard per-lavg was performed by injecting 5 mL sterile PBS into the peritoneal cavity that were subsequently harvested by performing an abdominal incision and collecting the resulting per-lavg directly onto a 15 mL tube using a glass funnel. In order to collect resMØ-aggregates, a ''strong'' per-lavg was performed. In this case a massage was applied to the abdomen prior to carrying out the abdominal incision and collecting the per-lavg, in order to promote the detachment of resMØ-aggregates from the mesothelium. resMØ-aggregates were subsequently isolated by sedimentation.

Cell suspensions

Cell suspensions from the per-lavg were obtained after centrifugation for 5 min at 400 g. To prepare cell suspensions from resMØ-aggregates, isolated resMØ-aggregates were digested with 0.05 mg/mL Liberase TL (Roche) and 0.25 mg/mL DNase I (Roche) in low glucose DMEM (Sigma-Aldrich) with 1% low fatty acid BSA, for 5 min at 37°C, washed and resuspended in EDTA-containing PBS supplemented with 3% FCS. To prepare omentum cell suspensions, the omentum was cut into small pieces, digested with 0.05 mg/mL Liberase TL and 0.25 mg/mL DNase I in low glucose DMEM with 1% low fatty acid BSA and 1M HEPES, for 25 min at 37°C, resuspended in DMEM supplemented with 3% FCS, filtered through 40-μm cell strainers, washed and resuspended in EDTA-containing PBS supplemented with 3% FCS. To prepare per-wall cell suspensions the per-wall was aseptically removed, cut into small pieces, digested with 0.18 mg/mL Liberase TM (Roche), 0.04 mg/mL DNase I and 0,5 mg/mL collagenase A in RPMI for 40 min at 37°C, resuspended in RPMI with 10% FCS, mechanically dissociated, filtered twice through 40-μm cell strainers, washed and resuspended in EDTA-containing PBS supplemented with 3% FCS after erythrocyte lysis by osmotic shock.

LPM purification

LPMs were isolated from per-lavg cell suspensions by negative selection after immunomagnetic depletion of B cells, SPMs, T cells and neutrophils with anti-rat immunoglobulin-coated magnetic beads (Thermo Fisher) at a 7:1 bead-to-cell ratio after incubation with antibodies anti MHC-II, CD90, Ly6C and Ly6G. After immunomagnetic depletion, LPM preparations had a purity > 90%.

Mesothelial cell isolation

The per-wall was aseptically removed and cut in two halves that were treated with 0.25% trypsin (Sygma) in 5mM EDTA-containing PBS, for 50 min at 37°C under continuous agitation. Intact tissues and cell debris were discarded and the resulting cell suspension was resuspended in EDTA-containing PBS with 3% FCS, filtered through a 40-μm cell strainer, washed and resuspended in EDTA-containing PBS with 3% FCS. Mesothelial cells were sorted as CD45$^-$ ICAM-1$^+$ cells using a FACSAria Fusion cell sorter (BD Biosciences).

Cytospin preparations

Cells were centrifuged onto glass slides by using a Shandon Cytospin 2, dry-fixed and stained with Giemsa (Sigma-Aldrich), or processed for immunofluorescent staining as described below. Images from Giemsa-stained slides were acquired using a Leica FDM2500 microscope (Leica). Quantification of bacteria internalized by macrophages was performed using ImageJ software (NIH, MD).

Analysis of serum enzymes

Alanine aminotransferase (ALT/GPT) and aspartate aminotransferase (AST/GOT) serum levels were determined using ALT and AST reagent kits (BioSystems), using a Benchmark Plus microplate spectrophotometer (Bio-Rad). Creatine kinase (CK) and lactate dehydrogenase (LDH) serum levels were determined using the Dimension clinical chemistry system (Siemens Healthcare Diagnostics)

LPM depletion

Clodronate-loaded liposomes and control PBS-loaded liposomes were purchased from Liposoma (Netherlands). LPM depletion was achieved by i.p. injection of 100 μL of clodronate-loaded liposomes; control mice were treated with 100 μL of PBS-loaded liposomes.

Neutrophil depletion

Mice were received two doses of 100 μg of anti-Gr1 antibody (clone RB6-8C5), anti-Ly6G antibody (clone 1A8, BioXCell) or isotype control antibody; the first dose was administered intraperitoneally 12 hours before infection; the second dose was administered intravenously 2 h before *E. coli* infection.

In vivo treatment with heparin and hirudin

Mice were injected intraperitoneally with 100 units of unfractionated heparin (Rovi) or 800 units of recombinant hirudin (Aniara Diagnostica), and infected simultaneously with *E. coli*.

In vitro LPM adherence assay

LPMs, purified as described above, were cultured overnight at 37°C at 1×10^5 cells/mL, in tissue culture-treated, flat-bottom 96-well plates, in complete RPMI 1640 medium supplemented with 10% FCS, in the absence or presence of 100 μg/mL huridin.

Transfer of peritoneal cells

2×10^6 total peritoneal cells obtained by per-lavg of LysM-eGFP mice were transferred intraperitoneally into B6 mice 24 h prior to *E. coli* infection.

In vivo cell fluorescent labeling

Mice were injected intraperitoneally, 24 h before *E. coli* infection, with 200 μL of the fluorescent dye Far-Red at 15μM, using the CellTrace Far Red Cell Proliferation Kit (Thermo Fischer) or with 200 μL of the fluorescent dye CFSE at 25 μM, using the Vybrant CFDA SE. Cell Tracer Kit (Invitrogen).

Cytokine and chemokine profiling

Relative levels of selected cytokines and chemokines were analyzed in 200 μL per-lavg samples using the Proteome Profiler Mouse Cytokine Array Kit, Panel A (R&D Systems) according to the manufacturer's protocol. TF was quantified using the Proteome Profiler Mouse XL Cytokine Array Kit (R&D Systems). The array membranes were scanned and spot signal intensity was quantified with the Protein Array Analyzer ImageJ Plugin.

Flow cytometry

Analysis of per-lavg, per-wall and omentum cell suspensions was performed after seven-color immunofluorescent staining. Fc receptors were blocked by incubation with an anti-CD16/32 antibody (clone 2.4G2) at 4°C for 15 min, and the cells were subsequently stained with fluorophore-conjugated or biotin-conjugated antibodies against the mouse antigens listed in the Key resources table, for 20 min at 4°C; incubation with biotin-conjugated antibodies was followed by incubation with fluorophore-conjugated streptavidin for 20 min at 4°C. Flow cytometry analysis of intracellular Gata6 was carried out by using eBioscience Foxp3/ Transcription Factor Staining buffer Set (Thermo Fischer). Analysis of intracellular Ki-67 expression was performed after cell surface labeling, by fixing and permeabilizing the cells using the BD Cytofix/Cytoperm kit, following the manufacturer's instructions (BD Biosciences). Analysis of cell death was performed, after cell surface labeling, using Annexin V and 7AAD, following the manufacturer's instructions (BioLegend). Data were acquired on a LSR II cytometer (BD Biosciences) and analyzed using FlowJo X software (Tree Star, Ashland, OR). The full list of antibodies used for flow cytometry can be found in the Key resources table.

Whole mount immunofluorescence (WMI)

Per-wall, omentum, gonadal fat, mesentery and colon samples were fixed in 4% paraformaldehyde for 15 min at RT. Blocking of unspecific binding of primary antibodies was performed by incubation in 2% BSA in PBS for 30 min at 4°C. Samples were then incubated with fluorophore-conjugated antibodies and DAPI (Sigma-Aldrich) for 2 h at 4°C. Alternatively, samples were incubated with

unconjugated-conjugated antibodies for 2 h at 4°C, followed by incubation with secondary antibodies and DAPI for 2 h at 4°C. Antibodies used for WMI staining are listed in the Key resources table. Staining with anti ZO-1 was performed after permeabilization with 0,1% Triton X-100 (Sigma-Aldrich) for 15 min at 4°C prior to incubation with antibodies. Whole organ samples were mounted with Mowiol (Hoechst) on μ-Dish 35 mm dishes with No. 1.5 ibidi Polymer Coverslips (ibidi). Images were acquired on a multispectral Leica TCS SP8 system confocal microscope and analyzed using ImageJ software (NIH, MD).

Immunofluorescent staining of cytospin slides

Air-dried cytospin slides were fixed in 4% paraformaldehyde for 15 min at RT and stained in humidity chambers. Blocking of unspecific binding of primary antibodies was performed by incubation in 2% BSA in PBS for 30 min at RT. Slides were treated with 0,1% Triton X-100 for 15 min at RT, incubated with fluorophore-conjugated antibodies, or unconjugated-conjugated antibodies for 1 h at 37°C followed by incubation with secondary antibodies and DAPI for 1 h at 37°C, and mounted with Mowiol. Antibodies used for immunofluorescence staining on cytospin slides are listed in the Key resources table. Images were acquired on a multispectral Leica TCS SP8 system confocal microscope and analyzed using ImageJ software (NIH, Bethesda, MD).

Electron microscopy

Samples of the per-wall and omentum were fixed with 1.5% glutaraldehyde and 1.5% paraformaldehyde in HEPES 0,15M pH7.4 for 1 h at RT and overnight at 4°C, postfixed with 1% osmium tetroxide (TAAB) in 0.1M Na-Cacodylate buffer for 2 h at 4°C and counterstained with 2% uranyl acetate for 1 h at 4°C. Samples were then dehydrated in graded acetone solutions and embedded in Epon-812 (TAAB). Semi-thin sections (1 μm) were obtained with a Leica EM UC6 ultramicrotome and stained with toluidine blue. Images were acquired with a Leica DM2500 microscope (Leica). Ultra-thin sections (80 nm) were obtained with a Leica EM UC6 ultramicrotome, and examined with a Jeol 1011 transmission electron microscope (Jeol).

Western blot

LPMs purified from per-lavgs obtained from unstimulated mice, or from mice at 30 and 60 min after intraperitoneal E.coli infection, were lysed in Cell Lysis Buffer with protease inhibitor cocktail (Sigma) and the serine protease inhibitor PMSF (Fluka). Protein extracts were quantified by Bradford measurement using the Bio-Rad protein assay (Bio-Rad), subjected to SDS–PAGE and transferred onto a nitrocellulose membrane (Bio-Rad Laboratories). The membranes were blocked with Tris-buffered saline Tween 20 (TBST) containing 5% nonfat dry milk for 1 h at RT and then incubated overnight at 4°C with primary antibodies against GSDMD (clone EPR20859, Abcam, # ab219800), Caspase-1 (Caspase-1 14F468, Santa Cruz Technology, sc-56036), IL-1β (IL-1β H-153, Santa Cruz Technology, sc-7884) or TF (Tissue Factor, R&D, AF3178). To detect TF, samples were analyzed under non reducing conditions. After being washed with TBST, the membranes were incubated with HRP-conjugated secondary antibodies (Cell Signaling) for 1 h at RT. The membranes were washed in TBST and analyzed using the ECL system (Amersham).

RNA extraction and real-time PCR

For real-time PCR analyses, RNA from purified FACS-sorted d0 LPMs and d1 moCs was extracted using the RNAqueous-Micro kit (Ambion). RNA was retro-transcribed using the High Capacity cDNA Reverse Transcription kit (Applied Biosystems). Real-time PCR was performed using 5x HOT FIREPol EvaGreen qPCR Mix Plus (Solis BioDyne, Tartu, Estonia) on an ABI PRISM 7900 Sequence Detection System (Applied Biosystems). Plg-RKT primers: F: GGCAAATGGCTATGCAGATCGC; R: AGGACCGAGAAAGGCTGGCTTC.

QUANTIFICATION AND STATISTICAL ANALYSIS

Data are presented as mean ± SD. Survival curve data are presented as a Kaplan-Maier plot with a log rank test used to compare susceptibility between the different groups. Data are judged to be statistically significant when $p < 0.05$ by two-tailed Student's t test. In figures, asterisks denote statistical significance (*, $p < 0.05$; **, $p < 0.01$; ***, $p < 0.001$). Statistical analysis was performed using Microsoft Excel or GraphPad PRISM 8 softwares.

Quantification of the area occupied by resMØ-aggregates (Figures 3E, 3Q, 7I, and 7V), omental milky spots (Figure 4I), and fibrin in resMØ-aggregates (Figure 7R) was performed using the ImageJ software.